

CRANFIELD UNIVERSITY

ANATOLE VERHAEGEN

**ACTIVE DAMPING OF MISSILE
BENDING VIBRATIONS**

SCHOOL OF AEROSPACE, TRANSPORT
SYSTEMS AND MANUFACTURING

MSc THESIS

CRANFIELD UNIVERSITY

SCHOOL OF AEROSPACE, TRANSPORT SYSTEMS AND
MANUFACTURING

MSc THESIS

Academic Year 2014-2015

Anatole Verhaegen

ACTIVE DAMPING OF MISSILE BENDING VIBRATIONS

Supervisor: Dr R. Żbikowski

August 2015

This thesis is submitted in partial (50%) fulfillment of the
requirements for the degree of Master of Science

©Cranfield University 2006. All rights reserved. No part of this publication
may be reproduced without the written permission of the copyright owner.

Abstract

To face increasing performance of aerial threats, defense missiles must be designed evermore agile. Bending vibrations have become a growing issue with slender missile airframes and are a primary source of low frequency noise for seekers. In the mean time, miniaturisation and cost reduction of sensors like gyroscopes and accelerometers make sensor-rich systems affordable. The study investigates how active damping of bending vibrations can be performed using multiple sensors on ASTER 30, an anti-missile missile.

A longitudinal servo-aeroelastic model for ASTER 30 is derived using flight dynamics equations and Euler-Bernoulli beam theory. A strain gauge, gyroscopes and accelerometers are placed at optimal locations to measure the missile bending state. These additional sensors are used to design three new autopilot architectures actively damping vibrations while controlling the lateral acceleration. These autopilots are tested on the model derived previously and compared with conventional non damping autopilots.

Additionally to giving a new look at vibrations alleviation on slender airframes, this thesis demonstrates a method to remove the structural filter in conventional autopilots and constructs a discussion around different types of low cost sensors that can be used for active structural damping.

Ackowledgments

Big up à toute la famille, wesh ! Zbla ! Hunhun ! Big up à toute la famille, wesh ! Zbla ! Hunhun ! Big up à toute la famille, wesh ! Zbla ! Hunhun ! Big up à toute la famille, wesh ! Zbla ! Hunhun ! Big up à toute la famille, wesh ! Zbla ! Hunhun ! Big up à toute la famille, wesh ! Zbla ! Hunhun ! Big up à toute la famille, wesh ! Zbla ! Hunhun ! Big up à toute la famille, wesh ! Zbla ! Hunhun ! Big up à toute la famille, wesh ! Zbla ! Hunhun ! Big up à toute la famille, wesh ! Zbla ! Hunhun ! Big up à toute la famille, wesh ! Zbla ! Hunhun !

Contents

Nomenclature	vi
List of Figures	vii
List of Tables	ix
1 Introduction	1
1.1 Motivations for Active Damping	1
1.2 Contributions to Knowledge	1
1.3 Thesis Structure	1
2 Literature Review and Preliminary Study	2
2.1 Literature Review	2
2.1.1 Structure Active Damping	2
2.1.2 Sensors for Structure Monitoring	2
2.1.3 Missile Actuations Systems	2
2.1.4 Sensors and Actuators Placement	2
2.2 Preliminary Study	2
3 Flexible Missile Modeling	3
3.1 Characteristics	3
3.2 Flight Dynamics	4
3.2.1 Mass Properties	4
3.2.2 Aerodynamics	4
3.2.2.1 Standard Atmosphere	4
3.2.2.2 Main Body Aerodynamics	4
3.2.2.3 Fins Aerodynamics	5
3.2.3 External Efforts	5
3.2.3.1 Frames	5
3.2.3.2 Gravity	6
3.2.3.3 Aerodynamic Efforts	6
3.2.3.4 Propulsion Efforts	7
3.2.4 Equations of Motion	7
3.2.4.1 Linear Acceleration	7

3.2.4.2	Pitching Moment Equation	8
3.2.5	Trim	8
3.2.6	State Space System	9
3.2.6.1	State Equation	10
3.2.6.2	Output Equation	11
3.3	Actuator Dynamics	12
3.4	Structural Model	12
3.4.1	From continuous to discrete	12
3.4.2	Second-Order Structural Model	16
3.4.2.1	Nodal Model	16
3.4.2.2	Modal Model	20
3.4.2.3	Output equation	22
3.4.3	Rigid-body Modes Elimination	24
3.4.4	State Space Model	26
3.4.4.1	From Second-Order Model to State Space Model	26
3.4.4.2	Formulation in State Space Modal Form 2	27
3.4.5	Model Reduction	28
3.5	Actuator & Sensor Placement	29
3.5.1	Actuator Placement	29
3.5.2	Sensor Placement	31
3.5.2.1	Placement Indices	31
3.5.2.2	Strain Gages Placement	32
3.5.2.3	Gyroscopes Placement	32
3.5.2.4	Accelerometers Placement	33
3.5.2.5	Outputs Selection	34
3.6	Flexible Missile Model	35
3.6.1	Structural and Flight Dynamics Interactions	36
3.6.2	Servo-Aeroelastic Model Inputs and Outputs	37
4	Active Damping Autopilots	38
4.1	Missile Control Inputs and Outputs	38
4.1.1	Actuators	38
4.1.2	Sensors	38
4.2	Lateral Acceleration Control	39
4.3	Vibrations Alleviation	39
4.3.1	Notch Filtering	40
4.3.2	Active Structural Damping	43
4.3.2.1	Requirements	43
4.3.2.2	Strain Feedback	43
4.3.2.3	Gyroscope Feedback	48
4.3.2.4	Accelerometer Feedback	48
4.4	H_∞ Fixed-Structure Tuning	51
4.5	Controllers Assessment and Comparison	55

4.5.1	Robustness to Uncertainty	55
4.5.2	Tracking	55
4.5.3	Actuators Demand	55
4.5.3.1	Demand for Lateral Acceleration	55
4.5.3.2	Parasitic Effects	58
4.5.4	Bending Reduction	59
4.5.4.1	Vibrations Alleviation	59
4.5.4.2	Dynamic Stress Alleviation	60
5	Results and Discussions	62
6	Conclusions	63
	References	64

Nomenclature

ρ_m	linear mass density
$\rho_{m_{booster}}$	linear mass density of the booster
$\rho_{m_{dart}}$	linear mass density of the dart
E_i	Young modulus of beam i
F_i	external force along z-axis applied on node i
G	center of gravity
$I_{G,y,i}$ or I_i	second moment of area of beam i
$I_{G,y_{booster}}$	second moment of area of the booster about the neutral axis along the y-axis
$I_{G,y_{dart}}$	second moment of area of the dart about the neutral axis along the y-axis
$I_{G,y}$	second moment of area about the neutral axis along the y-axis
L	missile length
l	length of an element beam
m	missile mass
m_i	mass of node i
$M_{y,i}$	external moment along y-axis applied on node i
n	number of nodes
E	longitudinal Young modulus of the missile

List of Figures

3.1	Flared Missile Lift and Pitching Moment Coefficients [5]	5
3.2	ASTER-30 Dimensions	13
3.3	Lumped Element Model of a Beam (5 nodes)	14
3.4	Computed First Mode Natural Frequency	15
3.5	Summary of Structural Parameters for 20 Nodes	15
3.6	Elementary Cases for Two Nodes	17
3.7	Modes Shape of ASTER-30	21
3.8	Bode plot of F_1 to $a_{z,75}$	27
3.9	Hankel Singular Values Decomposition - Strain Gages Output	29
3.10	Hankel Singular Values Decomposition - Gyroscopes Output	30
3.11	Hankel Singular Values Decomposition - Accelerometers Output	30
3.12	Placement Indices - Strain Gages	33
3.13	Placements Indices - Gyroscopes	34
3.14	Placement Indices - Accelerometers	35
3.15	Sensors Locations - Strain gages ε , Gyroscopes q and Accelerometers a_z	36
4.1	Latax Control Architecture	39
4.2	Root Locus of Pitch Rate Feedback	40
4.3	Root Locus of $\frac{q_{83}}{\theta_{Tref}}$	41
4.4	Bode Diagram of the Notch Filter	42
4.5	Bode Diagram of $\frac{q_{83}(s)}{\theta_{Tref}(s)}$	42
4.6	Closed-Loop with Notch Filter	43
4.7	Closed-Loop with Notch Filter	43
4.8	Bode Diagram of $\frac{\theta_T(s)}{\theta_{Tref}(s)}$	44
4.9	Bode Diagram of $\frac{\delta_F(s)}{\delta_{Fref}(s)}$	45
4.10	Block Diagram of Derivative Strain Feedback	45
4.11	Root Locus of $\frac{\varepsilon_{46}}{\delta_{Fref}}(s)$	46
4.12	Bode of $\frac{q_{83}}{\theta_{Tref}}(s)$ With and Without Strain Feedback	47
4.13	Feedback Architecture with Strain Gages	47
4.14	Root Locus of $\frac{\Delta q}{\delta_{Fref}}(s)$	49
4.15	Bode of $\frac{q_{83}}{\theta_{Tref}}(s)$ With and Without Δq Feedback	50
4.16	Feedback Architecture with Gyroscopes	50

4.17 Root Locus of $\frac{\Delta q}{\delta_{Fref}}(s)$	51
4.18 Bode of $\frac{q_{83}}{\theta_{Tref}}(s)$ With and Without $\sum a_z$ Feedback	52
4.19 Feedback Architecture with Accelerometers	52
4.20 Weighted Form for H_∞ -tuning	53
4.21 Poles of Closed Loop 1 to 5 Subject to Uncertainty	56
4.22 Step Reponse of a_{zref} to $(a_{zref} - a_{zCG})$	57
4.23 Sigma Plot of a_{zref} to $(a_{zref} - a_{zCG})$	57
4.24 Singular Values of a_{zref} to θ_T	58
4.25 Singular Values of a_{zref} to δ_F	59
4.26 Singular Values of θ_{Tpert} to θ_T	60
4.27 Singular Values of θ_{Tpert} to a_{z83v} (left) and q_{83v} (right)	61
4.28 Singular Values of θ_{Tpert} to ε_{46}	61

List of Tables

3.1	Natural Frequencies and Damping Ratios of Modes	22
4.1	H_∞ -tuned Controllers Parameters	54

Chapter 1

Introduction

1.1 Motivations for Active Damping

1.2 Contributions to Knowledge

1.3 Thesis Structure

Chapter 2

Literature Review and Preliminary Study

2.1 Literature Review

- 2.1.1 Structure Active Damping
- 2.1.2 Sensors for Structure Monitoring
- 2.1.3 Missile Actuations Systems
- 2.1.4 Sensors and Actuators Placement

2.2 Preliminary Study

Chapter 3

Flexible Missile Modeling

3.1 Characteristics

ASTER is the name of a family of missiles designed by Eurosam, a consortium between MBDA France, MBDA Italy and Thales Group. The family comprises ASTER 15 for short to medium range and ASTER 30 for short to long range in service since 2001. These missiles are composed of two parts: the booster and the terminal dart. The booster will bring the missile to the final altitude and close to the final speed of Mach 4.5, this phase is called the acceleration phase. When the solid propellant of the booster is completely burnt, the two stages separate and the dart will continue its way to the target.

ASTER 30 weights 450 kg for 4.9 m. The longitudinal acceleration is about 15 g. It can reach an altitude of 30 km and fly to up to Mach 4.5.

These missiles can generate lateral forces with two elements. The first being the thrust vectoring at the tail. Two nozzles are actuated with hydraulic cylinders and can orientate the thrust to generate pitching and yawing moments. The second element are fins at the tail of the dart. These fins are generally not used during the acceleration phase but will be in this study. The deflection of the fins can create a lateral force or a rolling moment. They also create little pitching and yawing moments because of their distance from the centre of gravity.

ASTER 30 is exceptionally slender and subject to bending. The link that binds the booster and the dart is thus very stiff and complex to maintain the two parts together under extreme bending moments. The study will investigate how to relax constraints on this link by damping bending oscillations that can damage the missile.

3.2 Flight Dynamics

3.2.1 Mass Properties

ASTER-30 has two parts. The booster weights $m_{booster} = 310\text{ kg}$ and will lose mass along the acceleration phase. However, it is considered that its mass is constant at 310kg to simplify the model. The dart weights $m_{dart} = 140\text{ kg}$ during the complete flight. The total mass of the missile is then $m = 450\text{ kg}$. With no more information on mass distribution, it is assumed that the mass is uniformly distributed in the booster and in the dart. The length of the booster is $L_{booster} = 2.2m$ and the dart is lightly longer with $L_{dart} = 2.7m$

The center of gravity G position is at $x_{CG} = \frac{\int x dm}{m}$. With the assumption on mass distribution,

$$x_{CG} = \frac{\frac{1}{2} L_{booster} m_{booster} + (L_{booster} + \frac{1}{2} L_{dart}) m_{dart}}{m}$$

that yields $x_{CG} = 1.86\text{ m}$.

The rotational inertia at the center of gravity and about the y-axis is $J_y = \int (x - x_{CG})^2 dm$ giving

$$J_y = \frac{1}{3} \frac{m_{booster}}{L_{booster}} [(L_{booster} - x_{CG})^3 + x_{CG}^3] + \frac{1}{3} \frac{m_{dart}}{L_{dart}} [(L_{dart} + L_{booster} - x_{CG})^3 - (L_{booster} - x_{CG})^3]$$

Finally $J_y = 789\text{ kg.m}^2$.

3.2.2 Aerodynamics

An aerodynamic model is needed to derive the equations of motion. The atmosphere and the variation of air density will first be defined, then the main body aerodynamics will be described ending with the fins aerodynamics.

3.2.2.1 Standard Atmosphere

For the atmosphere model, the International Standard Atmosphere is considered.

3.2.2.2 Main Body Aerodynamics

The reference surface for this kind of airframe is the cross-section of the missile. The bigger cross-section is at the booster and will be taken as reference surface. Thus $S_{ref} = \pi D_{booster}^2 / 4$. The length reference will be the largest diameter $L_{ref} = D_{booster}$.

ASTER-30 has a body which is very similar to the flared frame studied in [5]. Some of its aerodynamic data are in Figure 3.1. In this figure, the x-axis is oriented from nose to tail contrary to this thesis.

The lift coefficient slope in this paper is $C_{L\alpha} = 22\text{ rad}^{-1}$. Since the airframe is symmetric about its xy-plane, $C_{L0} = 0$. Similarly, the zero angle of attack pitching

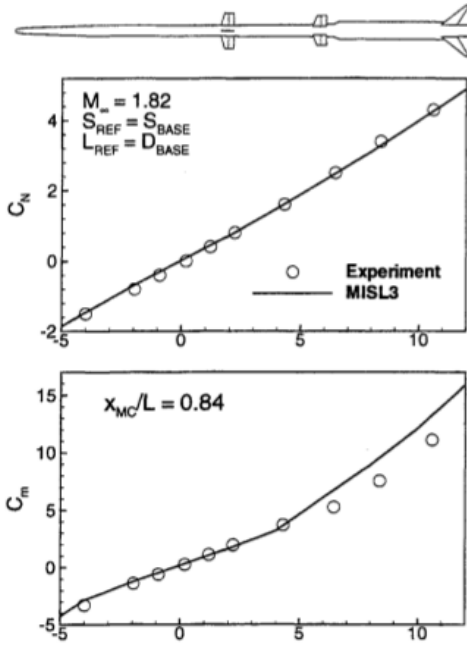


Figure 3.1: Flared Missile Lift and Pitching Moment Coefficients [5]

moment coefficient $C_{m0} = 0$. In this paper, the pitching moment coefficient slope is $C_{ma} = 45 \text{ rad}^{-1}$ at $x_{CM} = 0.78 \text{ m}$. However, this coefficient would place the aerodynamic center at $x_{AC} = \frac{L_{ref}C_{ma}}{C_{L\alpha}} + x_{CM} = 1.52 \text{ m}$. This aerodynamic center in this paper is too aft for this airframe compared to the center of gravity at $x_{CG} = 1.86 \text{ m}$. The aerodynamic center will be placed 7 cm aft of the center of gravity at $x_{AC} = 1.79 \text{ m}$. This yields a pitching moment coefficient slope of $C_{ma} = -4.3 \text{ rad}^{-1}$ **at the center of gravity**.

The drag coefficient for such a missile is given in [3]. The zero-lift drag is $C_{D0} = 0.95$ and the drag slope is estimated to be $k_D = 1$.

3.2.2.3 Fins Aerodynamics

3.2.3 External Efforts

Several external forces act on the missile airframe. These forces are due to gravity, aerodynamics and propulsion. It is important to describe clearly the frames in which they are defined.

3.2.3.1 Frames

There are four frames to define. They all have the axis $\vec{y}_0 = \vec{y}$ in common because the dynamics considered are only in the xz-plane.

The first one is the Earth's frame (\vec{z}_0, \vec{x}_0) where \vec{z}_0 is vertical and oriented downward. \vec{x}_0 is oriented forward.

The second one is the aerodynamic frame (\vec{z}_a, \vec{x}_a) with \vec{x}_a along the speed vector of the missile and \vec{z}_a normal to \vec{x}_a and oriented downward. The flight path frame is obtained by rotating the Earth's frame of an angle of γ the flight path angle around \vec{y} .

The third one is the body frame (\vec{z}_b, \vec{x}_b) where \vec{x}_b is along the body axis and \vec{z}_b normal to \vec{x}_b and oriented downward. The body frame is obtained by rotating the aerodynamic frame of an angle of α the angle of attack around \vec{y} . The pitch angle is $\theta = \alpha + \gamma$.

The last one is the propulsion frame (\vec{z}_T, \vec{x}_T) where \vec{x}_T is along the thrust vector and \vec{z}_T is normal to it and oriented downward. This last frame is obtained by rotating the body frame by an angle of θ_T - the nozzle angle - around \vec{y} .

3.2.3.2 Gravity

The gravity is assumed to be uniform during the flight and equal to the standard gravity value $g = 9.81 \text{ m.s}^{-2}$. Gravity is creating a force called weight applied at the center of gravity of the airframe and acting along the z-axis. This force is denoted \vec{W} and

$$\vec{W} = m g \vec{z}_0$$

3.2.3.3 Aerodynamic Efforts

The aerodynamic efforts can be divided into a lift force, a drag force and a pitching moment. The moment created by the lift and the drag is gathered into the pitching moment at the center of gravity.

Lift The lift is acting normal to the flight path along \vec{z}_a of amplitude L :

$$L = \frac{1}{2} \rho S_{ref} V^2 C_L$$

where $C_L = C_{L0} + C_{L\alpha}\alpha$.

Drag The drag is acting along the flight path \vec{x}_a and oriented opposite to the speed vector and of amplitude D .

$$D = \frac{1}{2} \rho S_{ref} V^2 C_D$$

with $C_D = C_{D0} + k_D C_L^2$.

Pitching Moment The pitching moment at the center of gravity is acting along the y-axis with an amplitude of M :

$$M = \frac{1}{2} \rho S_{ref} V^2 D_{ref} C_m$$

with $C_m = C_{m0} + C_{m\alpha}\alpha$.

3.2.3.4 Propulsion Efforts

The thrust is oriented along \vec{x}_T thanks to the orientable nozzle. The propulsion force is then

$$\vec{T} = T \vec{x}_T$$

3.2.4 Equations of Motion

The Equations of Motion are projected in the aerodynamic frame $(\vec{z}_a, \vec{x}_a, \vec{y})$. This gives three equations: the propulsion equation, the lift equation and the pitching moment equation.

3.2.4.1 Linear Acceleration

The linear acceleration of the center of gravity in an inertial frame of reference is linked to the sum of external forces by the mass of the airframe:

$$m \vec{a}_{CG/\mathcal{R}_e} = \sum \vec{F}_{external} \quad (3.1)$$

The acceleration in \mathcal{R}_e is

$$\vec{a}_{CG/\mathcal{R}_e} = \left[\frac{d\vec{V}}{dt} \right]_{\mathcal{R}_e}$$

The speed vector \vec{V} must be differentiated in the aerodynamic frame which is not an inertial frame of reference to link the acceleration with the aerodynamic parameters. The vector \vec{V} differentiated in the moving frame \mathcal{R}_a relative to the frame \mathcal{R}_e follows the following formula:

$$\left[\frac{d\vec{V}}{dt} \right]_{\mathcal{R}_e} = \left[\frac{d\vec{V}}{dt} \right]_{\mathcal{R}_a} + \vec{\Omega}_{\mathcal{R}_a/\mathcal{R}_e} \wedge \vec{V}$$

thus

$$\left[\frac{d\vec{V}}{dt} \right]_{\mathcal{R}_e} = \dot{V} \vec{x}_a - \dot{\gamma} V \vec{z}_a$$

Equation 3.1 is then projected in the aerodynamic frame (\vec{z}_a, \vec{x}_a) :

$$\begin{cases} m \dot{V} &= \sum \vec{F}_{external} \cdot \vec{x}_a \\ -m V \dot{\gamma} &= \sum \vec{F}_{external} \cdot \vec{z}_a \end{cases}$$

Finally, developping the sum of forces the first equation gives the propulsion equation:

$$m \dot{V} = -D + T \cos(\theta_T + \alpha) - W \sin(\gamma) \quad (3.2)$$

The second equation gives the lift equation:

$$-m V \dot{\gamma} = -L - T \sin(\theta_T + \alpha) + W \cos(\gamma) \quad (3.3)$$

3.2.4.2 Pitching Moment Equation

The pitching moment equation at the center of gravity along the y-axis is

$$J_y \dot{q} = \sum \vec{M}_{external}$$

Thus developping the pitching moment yields

$$J_y \dot{q} = M - T \sin(\theta_T) x_{CG} \quad (3.4)$$

3.2.5 Trim

At the trim state, the altitude is constant so $\gamma = \gamma_0 = 0 \text{ rad}$.

The speed of the missile is chosen to be Mach 2 at sea level and standard temperature, hence $V = V_0 = M a$. The speed of sound is

$$a = \sqrt{\gamma r T} = \sqrt{1.4 \cdot 287 \cdot (273.15 + 15)} = 340 \text{ m.s}^{-1}$$

Thus $V_0 = 680 \text{ m.s}^{-1}$ ($= 1322 \text{ kts}$).

The acceleration of the missile is said to be about 15g which corresponds to $\dot{V}_0 = 147 \text{ m.s}^{-2}$.

The altitude is said to be sea level then $\rho_0 = 1.21 \text{ kg.m}^{-3}$.

The other derivatives $\dot{\gamma}_0$, \dot{q}_0 , q_0 are zero.

Using the relation $\theta = \alpha + \gamma$, the Equations 3.2, 3.3 and 3.4 only unknowns at trim state are α_0 , T_0 and θ_{T0} . The solving of this system of equation gives the following result:

$$\begin{cases} \alpha_0 &= 0.030 \text{ rad} = 1.7^\circ \\ T_0 &= 71.3 \text{ kN} \\ \theta_{T0} &= -1.3 \cdot 10^{-3} \text{ rad} = 0.072^\circ \end{cases}$$

At this trim state, the lift is only $L = 2.4 \text{ kN}$ and the weight of the missile is $W = 4.4 \text{ kN}$ thus approximately half of it is lifted with the vertical component of

the thrust which is $T_0 \sin(\theta_{T0} + \alpha_0) = 2.0 \text{ kN}$. The drag is only $D = 5.0 \text{ kN}$ which corresponds to 7% of the thrust. The great majority of the thrust is generated for the acceleration. This gives an insight on the efforts magnitude applied on the airframe.

3.2.6 State Space System

The state vector considered for the state-space model is

$$x = \begin{bmatrix} \bar{\alpha} \\ q \end{bmatrix}$$

where q is the pitch rate and $\bar{\alpha}$ is the deviation of α from the trim value α_0 :

$$\bar{\alpha} = \alpha - \alpha_0$$

The state vector is only of dimension 2 because it is assumed that all the other variables like γ , $\dot{\gamma}$, V or ρ have a very slow dynamic. Indeed in study is interested about lateral acceleration generation, which happens faster than a change of navigation variables such as γ or V .

The input vector here is $u = \bar{\theta}_T$ which is the only parameter that the controller commands. $\bar{\theta}_T$ is the deviation of θ_T from θ_{T0} .

The output vector is

$$y = \begin{bmatrix} q \\ a_{zaCG} \\ a_{z_b10} \\ a_{z_b54} \\ a_{z_b83} \\ a_{z_b92} \end{bmatrix}$$

where a_{zaCG} is the inertial acceleration normal to the speed vector at the center of gravity, is the inertial acceleration normal to the body at node i and a_{z_bi} is the deviation of a_{z_bi} from the trim value a_{z_bi0} . Indeed, a_{z_bi0} is not zero at all. The missile is in constant acceleration at about 15g and has a trim angle of attack of $\alpha_0 = 0.030 \text{ rad}$, thus $a_{z_bi0} = 15 \cdot 0.030 = 0.45g$. Moreover a_{z_bi} will vary with a change in angle of attack because of the forward acceleration projected normally to the body. The missile onboard computer is probably able to subtract this component on the lateral acceleration. To simplify this problem that is not the purpose of the study, it will be assumed that $a_{z_bi} = a_{za_i}$. This means that an accelerometer fixed on the body is assumed to measure only the inertial acceleration normal to the speed vector. a_{za_i} will now be simply denoted a_{zi} . Thus

$$y = \begin{bmatrix} q \\ a_{zCG} \\ a_{z10} \\ a_{z54} \\ a_{z83} \\ a_{z92} \end{bmatrix}$$

The nodes are defined in Subsection 3.4.1 on page 12. The pitch rate q and acceleration a_{z83} are measured to control the rigid-body states of the missile. These measurements are already integrated in the current version of ASTER-30. The acceleration measurements at nodes 10, 54 and 92 will be used to measure the vibrations due to bending oscillations. The vibration components of these accelerations will be added later. The lateral acceleration of the center of gravity is measured to assess the system. Indeed, the controller will make this output equal to the reference acceleration.

3.2.6.1 State Equation

The two equations that governs the dynamic of this state-space system are Equations 3.3 and 3.4. Equation 3.3 can be rearrange using $\dot{\gamma} = q - \dot{\alpha}$ to give

$$\dot{\alpha} = \frac{1}{mV} \left(-\frac{1}{2} \rho S_{ref} V^2 (C_{L0} + C_{L\alpha} \alpha) - T \sin(\theta_T + \alpha) + W \cos(\gamma) \right) + q \quad (3.5)$$

Equation 3.4 yields

$$\dot{q} = \frac{1}{J_y} \left(\frac{1}{2} \rho S_{ref} V^2 L_{ref} (C_{m0} + C_{m\alpha} \alpha) - T \sin(\theta_T) x_{CG} \right) \quad (3.6)$$

The linearization of the two last Equations 3.5 and 3.6 about the trim state where $[\alpha, V, \rho, \theta_T, T, \gamma] = [\alpha_0, V_0, \rho_0, \theta_{T0}, T_0, \gamma_0]$. This bring the following matrix equation:

$$\begin{bmatrix} \dot{\bar{\alpha}} \\ \dot{q} \end{bmatrix} = A \begin{bmatrix} \bar{\alpha} \\ q \end{bmatrix} + B \bar{\theta}_T$$

where

$$A = \begin{bmatrix} A_{11} & A_{12} \\ A_{21} & A_{22} \end{bmatrix}$$

$$\begin{cases} A_{11} = -\frac{1}{mV_0} \left(\frac{1}{2} \rho_0 S_{ref} V_0^2 C_{L\alpha} + T_0 \cos(\theta_{T0} + \alpha_0) \right) \\ A_{12} = 1 \\ A_{21} = \frac{1}{J_y} \frac{1}{2} \rho_0 S_{ref} V_0^2 L_{ref} C_{m\alpha} \\ A_{22} = 0 \end{cases}$$

and

$$B = \begin{bmatrix} -\frac{T_0 \cos(\theta_{T0} + \alpha_0)}{m V_0} \\ -\frac{T_0 \cos(\theta_{T0}) x_{CG}}{J_y} \end{bmatrix}$$

A numerical computation gives the following results:

$$A = \begin{bmatrix} -0.498 & 1 \\ -7.22 & 0 \end{bmatrix}, \quad B = \begin{bmatrix} -0.233 \\ -168 \end{bmatrix}$$

3.2.6.2 Output Equation

The pitch rate q is already a state so adding this signal to the output is done easily.

The inertial acceleration a_{zCG} is normal to the speed vector and has been derived in Subsection 3.2.4.1 on page 7:

$$a_{zCG} = \frac{1}{m} (-L - T \sin(\theta_T + \alpha) + W \cos(\gamma))$$

Thus when linearized

$$a_{zCG} = -\frac{1}{m} \left(\frac{1}{2} \rho_0 S_{ref} V_0^2 C_{L\alpha} + T_0 \cos(\theta_{T0} + \alpha_0) \right) \alpha - \frac{T_0 \cos(\theta_{T0} + \alpha_0)}{m} \bar{\theta}_T$$

Given x the abscissa of a point on the missile, the lateral acceleration measured at this point will be

$$a_{z,x} = a_{z,CG} + (x_{CG} - x)\dot{q}$$

Hence using Equation 3.4 and linearizing

$$a_{z,x} = a_{z,CG} + \frac{1}{J_y} (x_{CG} - x) \left(\frac{1}{2} \rho_0 S_{ref} V_0^2 L_{ref} C_{m\alpha} \alpha - T_0 \cos(\theta_{T0}) x_{CG} \bar{\theta}_T \right)$$

For a node i , $x_i = (i - 1)l$.

This yields the output equation

$$y = C \begin{bmatrix} \bar{\alpha} \\ q \end{bmatrix} + D \bar{\theta}_T$$

The matrices C and D are

$$C = \begin{bmatrix} 0 & 1 \\ -\frac{1}{m} \left(\frac{1}{2} \rho_0 S_{ref} V_0^2 C_{L\alpha} + T_0 \cos(\theta_{T0} + \alpha_0) \right) & 0 \\ -\frac{1}{m} \left(\frac{1}{2} \rho_0 S_{ref} V_0^2 C_{L\alpha} + T_0 \cos(\theta_{T0} + \alpha_0) \right) + \frac{1}{J_y} (x_{CG} - 9l) \frac{1}{2} \rho_0 S_{ref} V_0^2 L_{ref} C_{m\alpha} & 0 \\ -\frac{1}{m} \left(\frac{1}{2} \rho_0 S_{ref} V_0^2 C_{L\alpha} + T_0 \cos(\theta_{T0} + \alpha_0) \right) + \frac{1}{J_y} (x_{CG} - 52l) \frac{1}{2} \rho_0 S_{ref} V_0^2 L_{ref} C_{m\alpha} & 0 \\ -\frac{1}{m} \left(\frac{1}{2} \rho_0 S_{ref} V_0^2 C_{L\alpha} + T_0 \cos(\theta_{T0} + \alpha_0) \right) + \frac{1}{J_y} (x_{CG} - 82l) \frac{1}{2} \rho_0 S_{ref} V_0^2 L_{ref} C_{m\alpha} & 0 \\ -\frac{1}{m} \left(\frac{1}{2} \rho_0 S_{ref} V_0^2 C_{L\alpha} + T_0 \cos(\theta_{T0} + \alpha_0) \right) + \frac{1}{J_y} (x_{CG} - 91l) \frac{1}{2} \rho_0 S_{ref} V_0^2 L_{ref} C_{m\alpha} & 0 \end{bmatrix}$$

$$D = \begin{bmatrix} 0 \\ -\frac{1}{m}T_0 \cos(\theta_{T0} + \alpha_0) \\ -\frac{1}{m}T_0 \cos(\theta_{T0} + \alpha_0) - \frac{1}{J_y}(x_{CG} - 9l)T_0 \cos(\theta_{T0}) x_{CG} \\ -\frac{1}{m}T_0 \cos(\theta_{T0} + \alpha_0) - \frac{1}{J_y}(x_{CG} - 52l)T_0 \cos(\theta_{T0}) x_{CG} \\ -\frac{1}{m}T_0 \cos(\theta_{T0} + \alpha_0) - \frac{1}{J_y}(x_{CG} - 82l)T_0 \cos(\theta_{T0}) x_{CG} \\ -\frac{1}{m}T_0 \cos(\theta_{T0} + \alpha_0) - \frac{1}{J_y}(x_{CG} - 91l)T_0 \cos(\theta_{T0}) x_{CG} \end{bmatrix}$$

Numerically this gives

$$C = \begin{bmatrix} 0 & 1 \\ -339 & 0 \\ -349 & 0 \\ -334 & 0 \\ -323 & 0 \\ -320 & 0 \end{bmatrix} \quad D = \begin{bmatrix} 0 \\ -158 \\ -397 \\ -30.3 \\ 211 \\ 286 \end{bmatrix}$$

3.3 Actuator Dynamics

The missile is directed with thrust vectoring. The two nozzles at the tail of the missile are mounted with hydraulic cylinders. The nozzles can be oriented to create a lateral component of thrust that will generate a moment. This moment will change the angle of attack of the missile to create a lateral acceleration.

The actuator is the limiting component in the control loop. Its bandwidth is estimated to be up to 25 Hz. The actuator dynamic is thus represented with a second order of cutoff frequency 25 Hz and damping ratio of 1:

$$H_{actuator}(s) = \frac{1}{40.5 \cdot 10^{-6}s^2 + 12.7 \cdot 10^{-3}s + 1}$$

3.4 Structural Model

3.4.1 From continuous to discrete

ASTER-30 length is 4.9 m and the largest diameter is 0.36 m on the booster so the missile can be considered as a beam with variable cross section. Euler-Bernoulli beam theory is suitable here because higher order models like Timoshenko beam theory would bring additive complexity and precision that are not needed for this study. Therefore sections rotational inertia and shear deformation are neglected. For the purpose of this study, only bending along y-axis is considered so deformations of the missile are contained in the zx-plane.

During the acceleration phase, ASTER-30 is composed of two parts: the booster and the dart. Both of them can be modeled as cylindrical pipes. The booster section

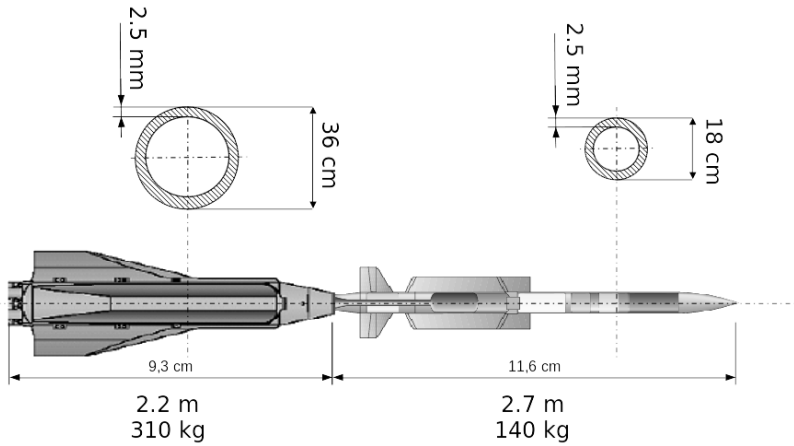


Figure 3.2: ASTER-30 Dimensions

has a diameter of 36 cm and the dart is 18 cm wide. The skin thickness¹ of the missile is 2.5 mm. These dimensions are illustrated in Figure 3.2.

The material used for the missile is assumed to be 30% carbon fibres composites and unidirectional along the longitudinal axis. The Young modulus along the x-axis is $E = 180 \text{ GPa}$ for such a material. The second moment of area at the neutral axis along y-axis for a cylindrical section is:

$$I_{G,y} = \pi \frac{D^4 - (D - 2e)^4}{64}$$

with D and e the external diameter and thickness of the pipe. Thus, the second moment of area for the booster and the dart are :

$$\begin{cases} I_{G,y_{booster}} &= 4.49 \cdot 10^{-5} \text{ m}^4 \\ I_{G,y_{dart}} &= 5.49 \cdot 10^{-6} \text{ m}^4 \end{cases}$$

It is assumed that the missile mass is equally distributed in the dart and in the booster therefore the linear mass density ρ_m is uniform in the booster, and uniform in the dart:

$$\begin{cases} \rho_{m_{booster}} &= 140.9 \text{ kg.m}^{-1} \\ \rho_{m_{dart}} &= 51.9 \text{ kg.m}^{-1} \end{cases}$$

It is necessary to discretize the body in order to be able to conduct a state-space representation and simulations. To reach this goal, the mathematical model of the structure is designed using a lumped element model illustrated in Figure 3.3.

¹Estimated from the natural frequency of the 1st bending mode at 20Hz

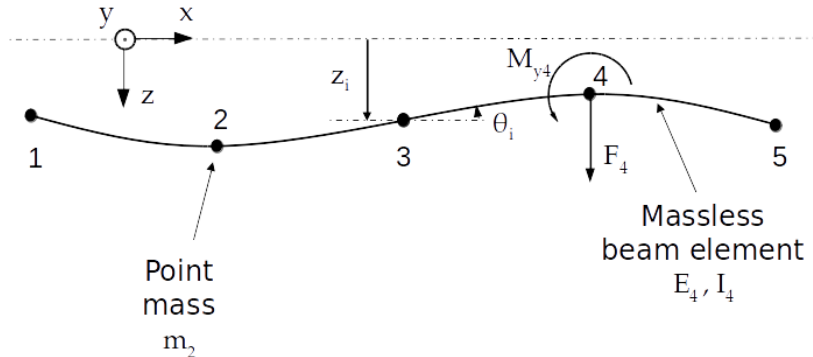


Figure 3.3: Lumped Element Model of a Beam (5 nodes)

Geometry The missile is longitudinally discretized in n nodes evenly spaced by the beams length $l = \frac{L}{n-1}$. The nodes i and $i + 1$ are linked together by a massless Euler-Bernoulli beam i . Let z_i , \dot{z}_i and \ddot{z}_i be respectively the displacement, speed and acceleration of node i along the z -axis. θ_i , $\dot{\theta}_i$ and $\ddot{\theta}_i$ are respectively the pitch angle, pitch rate and pitch acceleration of the beams at the junction node i .

To determine the number of nodes needed, we can consider looking at the natural frequencies of the beam converging as n grows. On Figure 3.4, first structural mode frequencies have been computed² for n varying between 7 and 300. The frequency converges when n increases. Eventually $n = 100$ is a good choice to minimize the number of nodes for computational efficiency and having an acceptable accuracy on natural frequencies. Indeed, at about $n = 100$, the frequency oscillates between 19.85 Hz and 20.15 Hz which corresponds to 1.5 % of variation. It is worth noting that the uncertainty on the real first mode frequency is 5 to 10 % so with $n = 100$, the first mode frequency can be said as converged.

Mass and stiffness Each node $i \in [1, n]$ has a point mass m_i that is the mass of the section from $x = (i - \frac{3}{2}) l$ to $x = (i - \frac{1}{2}) l$. Thus the mass is conserved during the discretization : $\sum_{i=1}^n m_i = m$. The Euler-Bernoulli beam i has a Young modulus E_i and the second moment of area at neutral axis passing through G and along y -axis $I_{G,y,i}$. For readability purposes, $I_{G,y,i}$ will be noted I_i but the reader must be carefull not to confuse it with a rotational inertia, generally noted J in this paper.

The different structural parameters of the body are summarized in Figure 3.5 for $n = 100$. It is clear that the booster is stiffer and heavier than the dart.

External efforts On each node i , an external force F_i along the z -axis and an external moment $M_{y,i}$ along the y -axis are applied.

²The method to do so will be explained later.

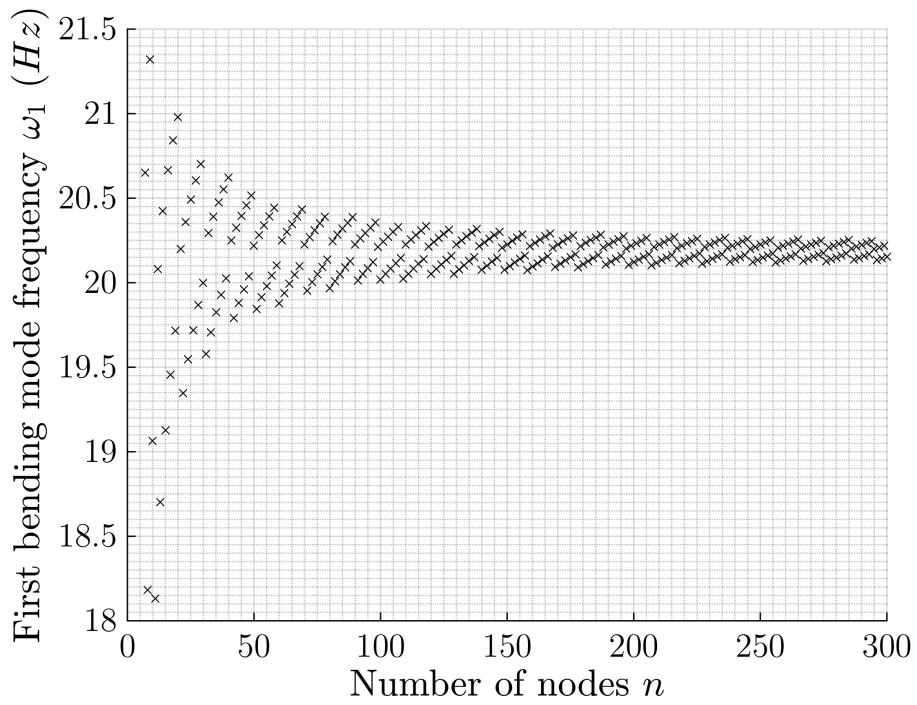


Figure 3.4: Computed First Mode Natural Frequency

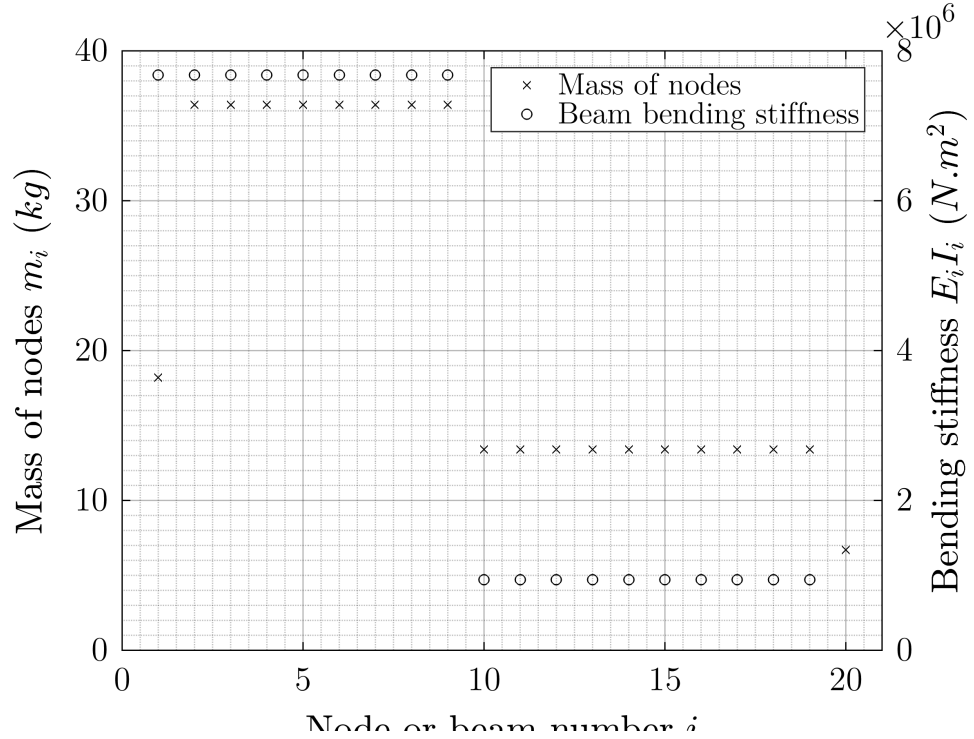


Figure 3.5: Summary of Structural Parameters for 20 Nodes

3.4.2 Second-Order Structural Model

3.4.2.1 Nodal Model

To generate a second-order structural model, Prentis and Leckie's method [6] will be used. This finite element model can be fully characterized by the following second-order structural equation:

$$M' \ddot{u} + D' \dot{u} + K' u = F' \quad (3.7)$$

- $u = \begin{bmatrix} z_1 \\ \vdots \\ z_n \\ \theta_1 \\ \vdots \\ \theta_n \end{bmatrix}$ is the displacement vector

- $F' = \begin{bmatrix} F_1 \\ \vdots \\ F_n \\ M_{y,1} \\ \vdots \\ M_{y,n} \end{bmatrix}$ is the external efforts matrix

- M' is the mass matrix of this system : $M' = \begin{bmatrix} M & 0_{n \times n} \\ 0_{n \times n} & J_y \end{bmatrix}$. M and J_y are diagonal matrices containing nodes masses and rotational inertias about the y-axis.
- K' and D' are the stiffness and damping matrices of this system.

K' can be divided in four sub-matrices $K' = \begin{bmatrix} K_{11} & K_{12} \\ K_{21} & K_{22} \end{bmatrix}$. In a static situation where \ddot{u} and \dot{u} are zero, the equation 3.7 becomes :

$$K' u = F' \quad (3.8)$$

Thus

$$\begin{bmatrix} K_{11} & K_{12} \\ K_{21} & K_{22} \end{bmatrix} \begin{bmatrix} z \\ \theta \end{bmatrix} = \begin{bmatrix} F \\ M_y \end{bmatrix}$$

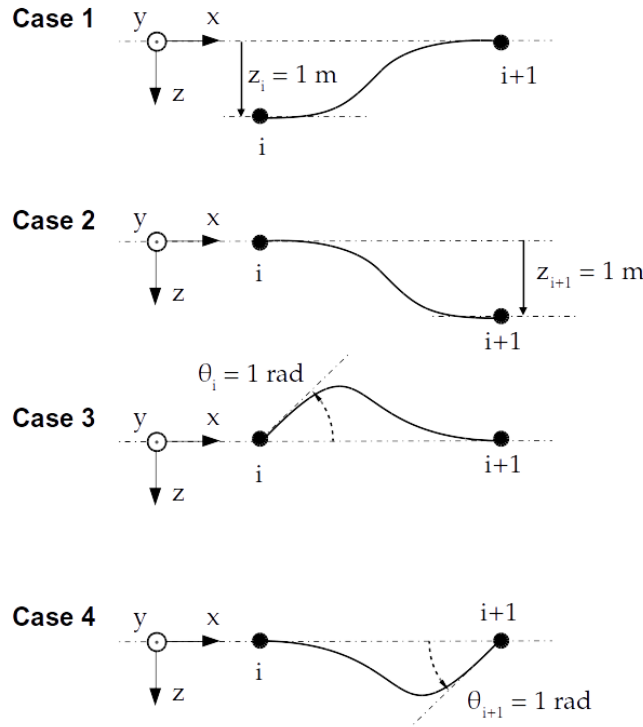


Figure 3.6: Elementary Cases for Two Nodes

Finding \$K'\$ To derive this matrix, one can consider only two nodes \$i\$ and \$i+1\$ linked with the beam \$i\$. The equation 3.8 is simplified to:

$$\begin{bmatrix} k_{11,i} & k_{12,i} \\ k_{21,i} & k_{22,i} \end{bmatrix} \begin{bmatrix} z_i \\ z_{i+1} \\ \theta_i \\ \theta_{i+1} \end{bmatrix} = \begin{bmatrix} F_i \\ F_{i+1} \\ M_{y,i} \\ M_{y,i+1} \end{bmatrix}$$

Four cases are considered and illustrated in Figure 3.6:

	\$z_i\$	\$z_{i+1}\$	\$\theta_i\$	\$\theta_{i+1}\$
Case 1	1	0	0	0
Case 2	0	1	0	0
Case 3	0	0	1	0
Case 4	0	0	0	1

The forces and moments applied to the beam are \$F_i\$, \$F_{i+1}\$, \$M_{y,i}\$ and \$M_{y,i+1}\$. The equilibrium between external efforts on the beam gives the two equations (forces and moments at node \$i\$):

$$F_i + F_{i+1} = 0 \quad (3.9)$$

$$M_{y,i} + M_{y,i+1} - l \cdot F_{i+1} = 0 \quad (3.10)$$

Using beam theory, the deformation and efforts are linked with the equation

$$E_i I_i \frac{\partial^2 z}{\partial x^2}(x) = -M_y(x) \quad (3.11)$$

where and $M_y(x) = M_{y,i+1} - (l - x) F_{i+1}$ are local young modulus, second moment of area and pitching moment at abscissa x ³. For readability purposes, $E_i I_i$ will now be noted EI_i . This yields after integration and double integration

$$EI_i \theta(x) = -\frac{1}{2}x^2 F_{i+1} + x (-M_{y,i+1} + l F_{i+1}) + A \quad (3.12)$$

$$EI_i z(x) = -\frac{1}{6}x^3 F_{i+1} + \frac{1}{2}x^2 (-M_{y,i+1} + l F_{i+1}) + A x + B \quad (3.13)$$

with A and B integration constants.

The boundary conditions are

$$\begin{cases} \theta(0) = \theta_i \\ \theta(l) = \theta_{i+1} \\ z(0) = z_i \\ z(l) = z_i \end{cases} \quad (3.14)$$

Thus, the system of equations 3.9, 3.10, 3.12, 3.13 and 3.14 for each case 1 to 4 yields :

	Case 1	Case 2	Case 3	Case 4
F_i	$12 EI_i / l^3$	$-12 EI_i / l^3$	$-6 EI_i / l^2$	$-6 EI_i / l^2$
F_{i+1}	$-12 EI_i / l^3$	$12 EI_i / l^3$	$6 EI_i / l^2$	$6 EI_i / l^2$
$M_{y,i}$	$-6 EI_i / l^2$	$6 EI_i / l^2$	$4 EI_i / l$	$2 EI_i / l$
$M_{y,i+1}$	$-6 EI_i / l^2$	$6 EI_i / l^2$	$2 EI_i / l$	$4 EI_i / l$

thus $k_{11,i}$, $k_{12,i}$, $k_{21,i}$ and $k_{22,i}$ derived from the table above are

$$\begin{cases} k_{11,i} &= \frac{12 EI_i}{l^3} \begin{bmatrix} 1 & -1 \\ -1 & 1 \end{bmatrix} \\ k_{12,i} = k_{21,i}^T &= \frac{6 EI_i}{l^2} \begin{bmatrix} -1 & -1 \\ 1 & 1 \end{bmatrix} \\ k_{22,i} &= \frac{2 EI_i}{l} \begin{bmatrix} 2 & 1 \\ 1 & 2 \end{bmatrix} \end{cases}$$

³ $x = 0$ at node i and $x = l$ and node $i + 1$

Now considering the complete missile, as the element beams are linked in serie, the matrices K_{11} , K_{12} , K_{21} , and K_{22} can be calculated by summing the matrices $k_{11,i}$, $k_{12,i}$, $k_{21,i}$ and $k_{22,i}$ on the diagonal as shown below for K_{11} :

$$K_{11} = \begin{bmatrix} k_{11,1} & & & & & \\ & k_{11,2} & & & & \\ & & k_{11,3} & & & \\ & & & k_{11,n} & & \\ & & & & k_{11,n-1} & \\ 0 & & & & & 0 \end{bmatrix}$$

Thus, these matrices are

$$K_{11} = \frac{12}{l^3} \begin{bmatrix} EI_1 & -EI_1 & 0 & \cdots & 0 \\ -EI_1 & EI_1 + EI_2 & \ddots & \ddots & \vdots \\ 0 & \ddots & \ddots & \ddots & 0 \\ \vdots & \ddots & \ddots & EI_{n-2} + EI_{n-1} & -EI_{n-1} \\ 0 & \cdots & 0 & -EI_{n-1} & EI_{n-1} \end{bmatrix}$$

$$K_{12} = K_{21}^T = \frac{6}{l^2} \begin{bmatrix} -EI_1 & -EI_1 & 0 & \cdots & 0 \\ EI_1 & EI_1 - EI_2 & \ddots & \ddots & \vdots \\ 0 & \ddots & \ddots & \ddots & 0 \\ \vdots & \ddots & \ddots & EI_{n-2} - EI_{n-1} & -EI_{n-1} \\ 0 & \cdots & 0 & EI_{n-1} & EI_{n-1} \end{bmatrix}$$

$$K_{22} = \frac{2}{l} \begin{bmatrix} 2EI_1 & EI_1 & 0 & \cdots & 0 \\ EI_1 & 2EI_1 + 2EI_2 & \ddots & \ddots & \vdots \\ 0 & \ddots & \ddots & \ddots & 0 \\ \vdots & \ddots & \ddots & 2EI_{n-2} + 2EI_{n-1} & EI_{n-1} \\ 0 & \cdots & 0 & EI_{n-1} & 2EI_{n-1} \end{bmatrix}$$

It is worth noting that $K' = K'^T$ that can be explained by Maxwell-Betti reciprocal work theorem.

Simplified second-order structural model In this study, we assume that the pure external moments $M_{y,i}$ are negligible when compared to moments created by the forces F_i . The missile is modeled as an Euler-Bernoulli beam, thus the local rotational inertias I_i are zero. The damping D' is very few for such flexible structures so it can be neglected

for the next trick. With these hypotheses, the lower part of Equation 3.7 concerning rotational acceleration becomes :

$$0_{n \times 1} \ddot{\theta} + 0_{n \times 1} \dot{\theta} + K_{21}z + K_{22}\theta = 0_{n \times 1}$$

K_{22} is a symmetric tridiagonal matrix which invertibility can be proven by LU decomposition[2]. This leads to the important relation between z and θ :

$$\theta = -K_{22}^{-1} K_{21}z \quad (3.15)$$

This equation mean that the second part of u can be entirely determined from its first part. The upper part of the Equation 3.7 fully describes the structural system:

$$M \ddot{z} + D \dot{z} + (K_{11} - K_{12}K_{22}^{-1}K_{21}) z = F$$

The stiffness matrix is then $K = K_{11} - K_{12}K_{22}^{-1}K_{21}$. One can verify that $K^T = K$.

The damping matrix is chosen proportionnal to K and set to damp the first structural mode to 1%. This gives $D = K/6000$. The second-order structural equation is as follows:

$$M \ddot{z} + D \dot{z} + K z = F \quad (3.16)$$

3.4.2.2 Modal Model

The triplet (M, D, K) is the nodal realization of the second-order structural model. A modal realization must be found to extract the flexible body modes from the structural model. The transformation of the nodal model is described in [4] and can be derived as follows.

Considering free vibrations without damping, the system being linear, the displacement vector will be $z = \phi e^{j\omega t}$ with ϕ constant thus $\ddot{z} = -\omega^2 \phi e^{j\omega t}$ and Equation 3.16 becomes:

$$(-\omega^2 M + K) \phi = 0 \quad (3.17)$$

Non-trivial solutions to Equation 3.17 (i.e. $\phi \neq 0$) exist if and only if

$$\det(-\omega^2 M + K) = 0$$

The solutions are the generalized eigen values $(\omega_1^2, \omega_2^2, \dots, \omega_n^2)$ of the matrices K and M . $(\omega_1, \omega_2, \dots, \omega_n)$ are the natural frequencies of the structure and the eigen vectors $(\phi_1, \phi_2, \dots, \phi_n)$ are the natural modes also called modes shape.

In this particular study, the structure extremities are free hence the two first natural frequencies are 0 Hz and the two first natural modes correspond to the rigid-body modes: z-axis translation and y-axis rotation. The natural frequencies and modes shape are renamed $(0, 0, \omega_1, \omega_2, \dots, \omega_{n-2})$ and $(\phi_{0,1}, \phi_{0,2}, \phi_1, \phi_2, \dots, \phi_{n-2})$.

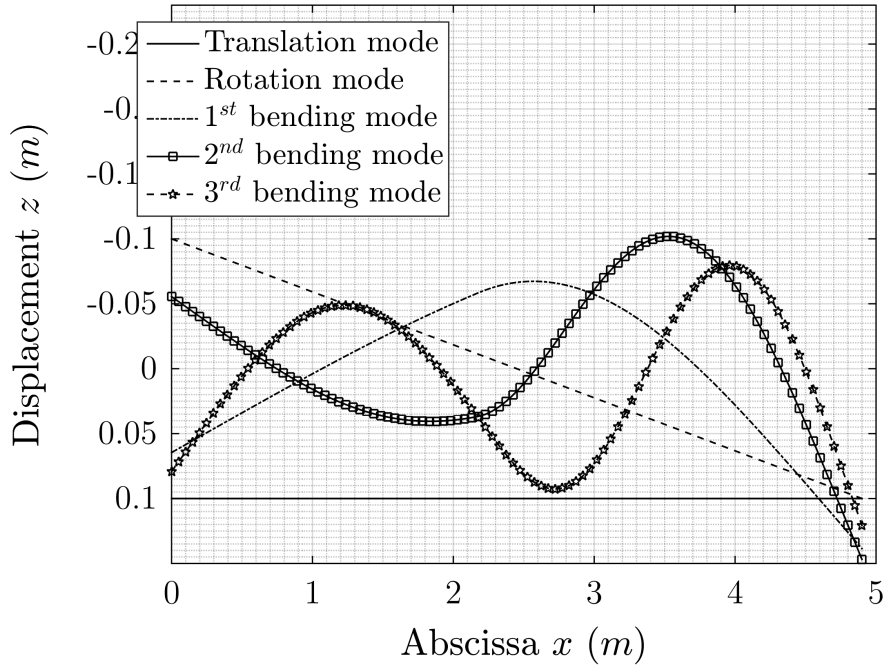


Figure 3.7: Modes Shape of ASTER-30

The modes shape of the rigid-body and the first three bending modes are plotted in Figure 3.7. This figure shows that the dart is likely to bend more than the booster. Indeed, the front part of the missile is more flexible so it will bend more.

The natural frequencies for the first modes are summarized in Table 3.1.

Let $\Phi = [\phi_{0,1} \phi_{0,2} \phi_1 \phi_2 \dots \phi_{n-2}]$ be the modal matrix and

$$\Omega = \begin{bmatrix} 0 & & & \\ & 0 & & 0 \\ & & \omega_1 & \\ & & & \ddots \\ 0 & & & \omega_{n-2} \end{bmatrix}$$

be the matrix of natural frequencies.

Let z_m be the displacement vector of modes defined by $z = \Phi z_m$. The modal matrices of mass M_m , damping D_m and stiffness K_m are obtained as follows

$$M_m = \Phi^T M \Phi$$

$$D_m = \Phi^T D \Phi$$

$$K_m = \Phi^T K \Phi$$

Mode	Natural Frequency		Damping Ratio
	(Hz)	(rad.s ⁻¹)	
z translation mode	0	0	0
y rotation mode	0	0	0
1 st bending mode	20.0	125	1.0%
2 nd bending mode	67.7	425	3.5%
3 rd bending mode	139.7	877	7.3%
4 th bending mode	213.9	1344	11%
5 th bending mode	335.1	2106	17%

Table 3.1: Natural Frequencies and Damping Ratios of Modes

The triplet (M_m, D_m, K_m) defines the second-order structural modal model of the missile. The equation 3.16 becomes:

$$M_m \ddot{z}_m + D_m \dot{z}_m + K_m z_m = \Phi^T F \quad (3.18)$$

3.4.2.3 Output equation

Three types of sensors are investigated in this paper to measure vibrations: strain gages, gyroscopes and accelerometers. Their measurement can be represented by the output equation:

$$y = C_{oz}z + C_{ov}\dot{z} + D_oF \quad (3.19)$$

where y is a vector containing the measurement of all sensors.

It means that the signal measured by the sensors are a linear combination of the displacement of the nodes (matrix C_{oz}), their speed (matrix C_{ov}) and also a feedforward term D_o on the external forces applied on the nodes.

Gyroscope A gyroscope on node i measures $\dot{\theta}_i$, thus n gyroscopes can be placed. Since q is often used to represent the pitch rate, this letter will be used for gyroscope output matrices. According to Equation 3.15, $\theta = -K_{22}^{-1}K_{21}z$, therefore $\dot{\theta}_i = -K_{22}^{-1}K_{21}\dot{z}$. This yields the output matrices

$$C_{ozq} = 0_{n \times n} \quad C_{ovq} = -K_{22}^{-1}K_{21} \quad \text{and} \quad D_{oq} = 0_{n \times n}$$

Accelerometer An accelerometer on node i measures \ddot{z}_i . The letter assigned to acceleration measurement will be a like “acceleration” and the measurement will be called a_z . With an accelerometer on each node, there are n accelerometers. In Equation 3.19, \ddot{z} does not appear. But using the second-order structural equation 3.16:

$$\ddot{z} = -M^{-1}Kz - M^{-1}D\dot{z} + F$$

thus

$$C_{oza} = -M^{-1}K \quad C_{ova} = -M^{-1}D \quad \text{and} \quad D_{oa} = Id_n$$

Strain gage For a strain gage, a first order Taylor developpement to approximate the spatial derivative of $\theta(x)$ at node i will be conducted. This approximation cannot be made on nodes 1 and n therefore, only $n - 2$ strain gages are considered. The letter used for this sensor is ε which is often assigned to strains.

The Euler-Bernoulli beam theory assumes that each section stays perpendicular to the neutral axis. The strain gages are placed on the upper side of the missile therefore, the local deformation at the surface is

$$\varepsilon(x) = -\frac{\partial \theta}{\partial x} \frac{D(x)}{2}$$

where $D(x)$ is the local missle diameter. It is worth noting that $\varepsilon(x)$ is positive when the strain gage is stretched and negative when it is compressed.

The partial derivative of θ with respect to x is approximated using a first order Taylor developpement at node $i \in [2, n-1]$:

$$\frac{\partial \theta}{\partial x}(x_i) \simeq \frac{\theta_{i+1} - \theta_{i-1}}{2l}$$

thus

$$\varepsilon_i = \frac{-\theta_{i+1} + \theta_{i-1}}{2l} \frac{D_i}{2}$$

Let $\varepsilon = (\varepsilon_i)_{i \in [2, n-1]}$, then the previous equation yields

$$\varepsilon = T_\varepsilon \theta$$

with

$$T_\varepsilon = \frac{1}{4l} \begin{bmatrix} D_2 & 0 & -D_2 & & & & 0 \\ & D_3 & 0 & -D_3 & & & \\ & & D_4 & 0 & -D_4 & & \\ & & & \ddots & \ddots & \ddots & \\ & & & & D_{n-2} & 0 & -D_{n-2} \\ 0 & & & & & D_{n-1} & 0 & -D_{n-1} \end{bmatrix}$$

Finally, using Equation 3.15, the relation becomes

$$\varepsilon = -T_\varepsilon K_{22}^{-1} K_{21} z$$

hence

$$C_{oz\varepsilon} = -T_\varepsilon K_{22}^{-1} K_{21} \quad C_{ov\varepsilon} = 0_{(n-2) \times n} \quad \text{and} \quad D_{o\varepsilon} = 0_{(n-2) \times n}$$

Concatenation The output vector corresponding to the concatenation of all measurements is $y = \begin{bmatrix} \varepsilon \\ q \\ a_z \end{bmatrix}$. Therefore

$$C_{oz} = \begin{bmatrix} C_{oz\varepsilon} \\ C_{ozq} \\ C_{oza} \end{bmatrix} \quad C_{ov} = \begin{bmatrix} C_{ov\varepsilon} \\ C_{ovq} \\ C_{ova} \end{bmatrix} \quad \text{and} \quad D_o = \begin{bmatrix} D_{o\varepsilon} \\ D_{oq} \\ D_{oa} \end{bmatrix}$$

Modal output matrix The Output Equation 3.19 will finally be

$$y = C_{oz}\Phi z_m + C_{ov}\Phi \dot{z}_m + D_o F$$

defining the modal equivalent of the output matrices :

$$y = C_{mz}z_m + C_{mv}\Phi \dot{z}_m + D_o F$$

with

$$\begin{cases} C_{mz} &= C_{oz}\Phi \\ C_{mv} &= C_{ov}\Phi \end{cases}$$

3.4.3 Rigid-body Modes Elimination

The second-order structural model and its output equation in there modal forms have been derived. However, the two rigid-body modes - translation and rotation - must be eliminated. Indeed, this Chapter aims at modeling only vibrations during the flight. The rigid-body dynamics modeled have been derived isolated from gravity and air and do not reflect flight dynamics hence they must be suppressed to keep only vibrations dynamics.

The matrices M_m , D_m and K_m are diagonal meaning that there is no interaction between modes in Equation 3.18. The rigid-body modes are eliminated by erasing the two first rows of Φ . Hence it is now $\Phi = [\phi_1 \phi_2 \dots \phi_{n-2}]$ and z_m only contains structural modes displacement. By doing so, modal mass, damping and stiffness matrices size is now $(n - 2) \times (n - 2)$.

Looking at the output Equation 3.19, truncating the rigid-body modes will remove rigid-body pitch rate and strain measurement is not influenced by rigid-body modes. However, great care must be taken for the acceleration measurement as $D_{oa} \neq 0$. To compute the acceleration measurements only due to the vibrations, the acceleration measurements due to the rigid-body modes will be calculated considering a rigid structure.

If the missile is considered as a solid, the equation of lateral acceleration at the center of gravity is:

$$a_{z,CG} = \frac{1}{m}F_z$$

and the equation of rotational acceleration is

$$\ddot{\theta} = \frac{1}{J_{y,CG}} M_{y,CG}$$

where F_z is the sum of external forces along the z-axis, $M_{y,CG}$ is the sum of moments applied at the center of gravity along the y-axis, m and J_y are the mass and rotational inertia about the center of gravity along the y-axis. The force and moments are:

$$F_z = \sum_{j=1}^n F_j$$

$$M_{y,CG} = \sum_{j=1}^n (x_{CG} - x_j) F_j$$

The acceleration at each node i is

$$a_{z,i} = a_{z,CG} + (x_{CG} - x_i) \ddot{\theta}$$

Hence, it yields

$$a_{z,i} = \frac{1}{m} \sum_{j=1}^n F_j + (x_{CG} - x_i) \frac{1}{J_y} \sum_{j=1}^n (x_{CG} - x_j) F_j$$

In matrix formulation,

$$a_{z,rb} = D_{oa,rb} F$$

where

$$D_{oa,rb} = \frac{1}{m} Id_n + \frac{1}{J_y} \begin{bmatrix} x_{CG} \\ x_{CG} - l \\ \vdots \\ x_{CG} - (n-2)l \\ x_{CG} - (n-1)l \end{bmatrix} \begin{bmatrix} x_{CG} & x_{CG} - l & \dots & x_{CG} - (n-2)l & x_{CG} - (n-1)l \end{bmatrix}$$

Finally, the output matrix $D_{oa,rb}$ is subtracted from D_{oa} to obtain the output matrix from vibrations only :

$$D_{oa,fb} = D_{oa} - D_{oa,rb}$$

However, this is not completely correct. Indeed, the rigid-body dynamics are different when the missile is considered as flexible. Therefore the rigid-body component in D_{oa} is not $D_{oa,rb}$. Looking at the Bode plot of the transfer function⁴ from F_1 to $a_{z,75}$

⁴Established later

on Figure 3.8, with this first rigid-body subtraction technique, at $\omega = 0$, $a_{z,75}(\omega)$ is not zero (curve “a_z,fb imperfect”). This is incorrect because at $\omega = 0$, the vibrations are not excited then they should be inexistant and $a_{z,75} = 0$. Once the state space representation will be established, the good correction will be applied.

3.4.4 State Space Model

Previously, the second-order structural model in its modal form without the rigid-body modes has been derived. This representation is not convenient for control design. Therefore a state-space representation of this system will be created.

3.4.4.1 From Second-Order Model to State Space Model

The system must firstly be translated into a state space representation.

Now that the rigid-body modes are eliminated, K_m is positive-definite and we can define

$$\Omega = M_m^{-1/2} K_m^{1/2}$$

$$Z = \frac{1}{2} M_m^{-1} D_m \Omega^{-1}$$

Z is a diagonal matrix containing the modes damping ratios. For instant $Z_{3,3} = \zeta_3$ is the damping ratio of the third bending mode.

The state vector is defined as $x = \begin{bmatrix} z_m \\ \dot{z}_m \end{bmatrix}$. The input vector is $u = F$. The ouput vector is $y = \begin{bmatrix} \varepsilon \\ q \\ a_z \end{bmatrix}$. Thus

$$\dot{x} = Ax + Bu$$

$$y = Cx + Du$$

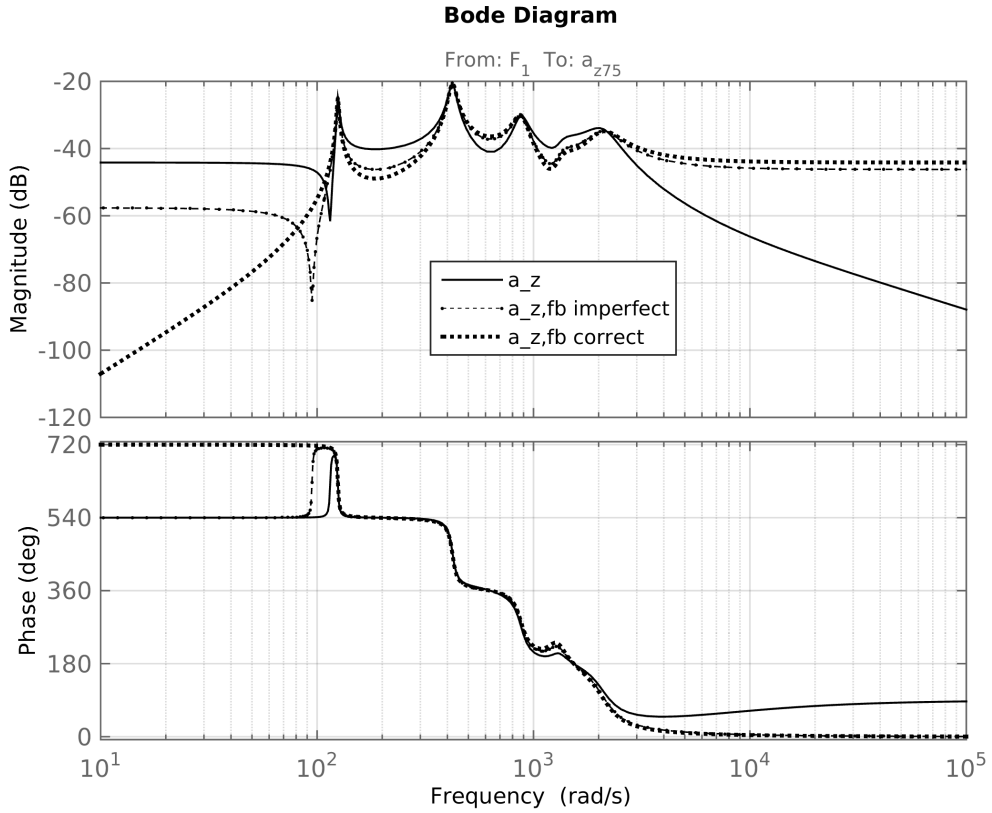
with

$$A = \begin{bmatrix} 0_{(n-2) \times (n-2)} & Id_{n-2} \\ -\Omega^2 & -2Z\Omega \end{bmatrix}$$

$$B = \begin{bmatrix} 0_{(n-2) \times n} \\ \Phi^T \end{bmatrix}$$

$$C = [C_{mz} \quad C_{mv}]$$

$$D = D_o = \begin{bmatrix} 0_{(n-2) \times n} \\ 0_{n \times n} \\ D_{oa,fb} \end{bmatrix}$$


 Figure 3.8: Bode plot of F_1 to $a_{z,75}$

In the previous part, $D_{oa,fb}$ has not been clearly defined. To eliminate properly rigid-body dynamics measured by acceleration sensors, the following technique can be used. The acceleration due to rigid-body dynamics is composed of a feedforward term $D_{oa,rb}$ only. In the transfer function, this is a static gain. Thus, one can just remove this static value :

$$a_z(j\omega) = -C_{ma}(A - j\omega Id)^{-1}B + D_{oa,fb}$$

where $C_{ma} = [C_{mza} \ C_{mva}]$. At $\omega = 0$, $a_z = 0$ so $D_{oa,fb} = C_{ma}A^{-1}B$.

Thanks to this, a_z is 0 at low frequency as shown in Figure 3.8 (curve “a_{z,fb} correct”).

3.4.4.2 Formulation in State Space Modal Form 2

Gawronski [4] gives a convenient state space formulation of the structural system. It is the modal form 2. In this form, the state vector is

$$x_m = \begin{bmatrix} z_{m,1} \\ z_{mo,1} \\ z_{m,2} \\ z_{mo,2} \\ \vdots \\ z_{m,(n-2)} \\ z_{mo,(n-2)} \end{bmatrix}$$

where $z_{mo,i} = \zeta_i z_{m,i} + \dot{z}_{m,i}/\omega_i$. In this form, the modal state matrix A_m has the particular form:

$$A_m = \begin{bmatrix} A_{m1} & & & \\ & A_{m2} & & \\ & & \ddots & \\ & & & A_{m(n-2)} \end{bmatrix}$$

$$\text{with } A_m = \begin{bmatrix} -\zeta_i \omega_i & \omega_i \\ \omega_i & -\zeta_i \omega_i \end{bmatrix}.$$

The transformation matrix V_m defined as $x = V_m x_m$ for 4 modes is

$$V_m = \begin{bmatrix} 1 & 0 & & & \\ & 1 & 0 & & \\ & & 1 & 0 & \\ & & & 1 & 0 \\ -\omega_1/\zeta_1 & \omega_1 & & & \\ & -\omega_2/\zeta_2 & \omega_2 & & \\ & & -\omega_3/\zeta_3 & \omega_3 & \\ & & & -\omega_4/\zeta_4 & \omega_4 \end{bmatrix}$$

Hence, $B_m = BV_m$, $C_m = CV_m$ and $D_m = D$.

This final state-space realization (A_m, B_m, C_m, D_m) is the modal state-space model of the vibrations of the missile with outputs y containing $n - 2$ strain measurements ε_i , n gyroscope measurements q_i and n accelerometers a_{zi} . This vibrations model will then be added to the flight dynamics model.

3.4.5 Model Reduction

Currently, the structural model has $n - 2$ bending modes. The number of nodes chosen is 100 so 98 modes are considered. Most of the high frequency modes are inaccurate because of the Euler-Bernoulli model which is suitable for low frequency dynamics. Fortunately, these modes do not contribute much to the system dynamics. A way to compare every mode contribution is to use the Hankel singular values decomposition of the system. On Figures 3.9, 3.10, 3.11, the state contribution in the Hankel singular values have been plotted for the three different types of sensor. The state vector is

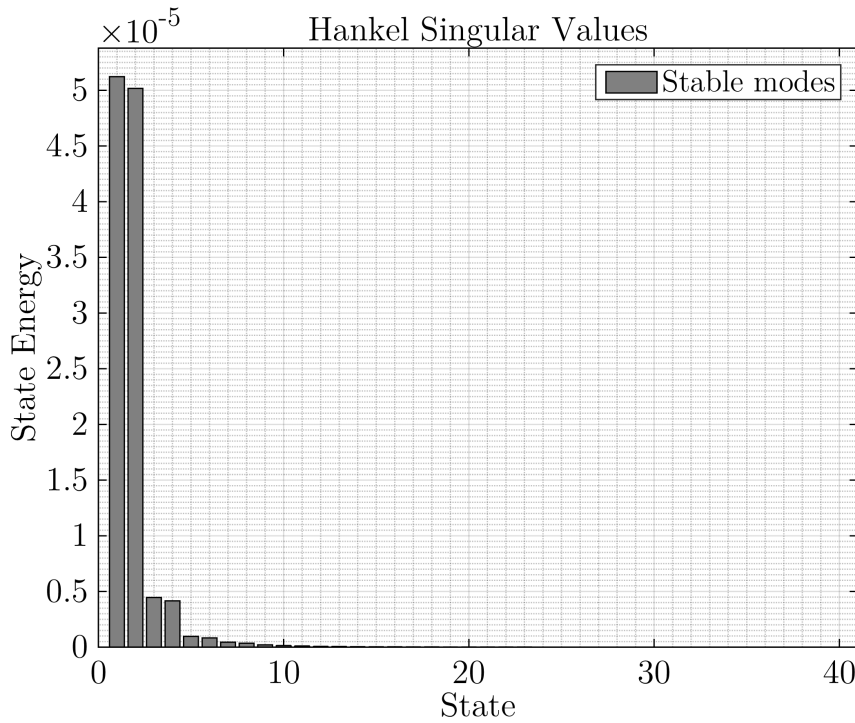


Figure 3.9: Hankel Singular Values Decomposition - Strain Gages Output

$x_m = \begin{bmatrix} q_{mi} \\ q_{moi} \end{bmatrix}_i$. The first five bending modes will be kept, the others are truncated.

Indeed, on these bar plots, the contribution of the 6th bending mode (bar 10 and 11) and higher (12 and above) is negligible. These modes correspond to less than 0.5% of the singular value of the 1st mode for the strain gages, less than 1% for the gyroscopes and 5% for the accelerometers.

To reduce the model to the five first modes, the new state space model is $(A_m^5, B_m^5, C_m^5, D_m^5)$. A_m^5 is the 10×10 upper left corner of A_m , B_m^5 is the 10 first rows of B_m , C_m^5 is the 10 first columns of C_m and D_m^5 is equal to D_m .

From now on, $(A_m^5, B_m^5, C_m^5, D_m^5)$ will be simply named (A, B, C, D) .

3.5 Actuator & Sensor Placement

3.5.1 Actuator Placement

The goal of this paper is to enhance the global performance of ASTER-30 by adding sensors. No actuators from the original model will be added hence the only actuators available are the thrust vectoring by nozzle orientation at the very rear of the missile and the fins at the tail of the dart. The position of these two actuators on the airframe are $x_{nozzle} = 0\text{ m}$ and $x_{fins} = 2.4\text{ m}$. These positions corresponds to the nodes 1 and

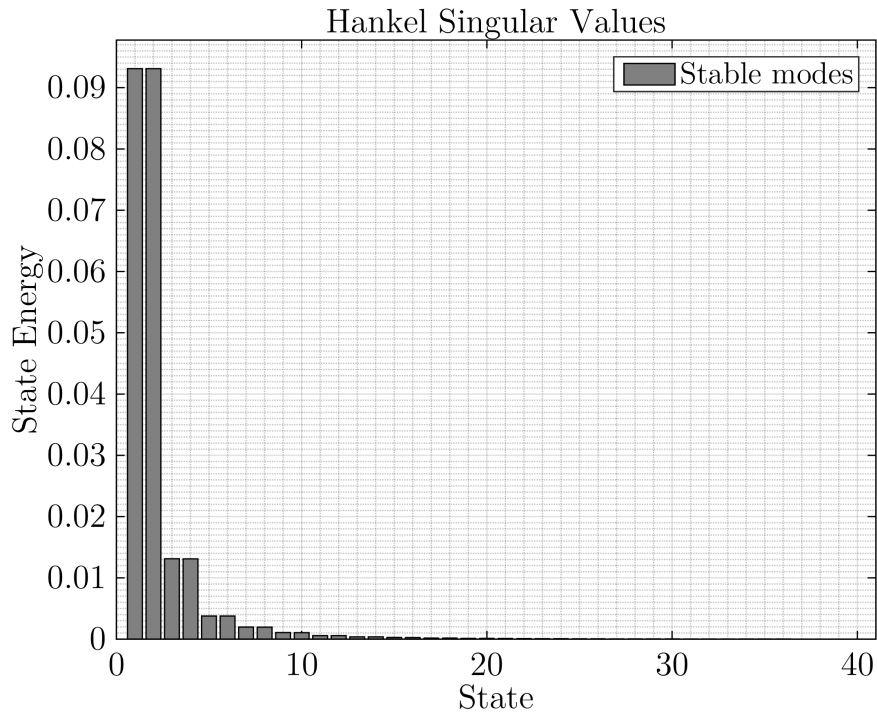


Figure 3.10: Hankel Singular Values Decomposition - Gyroscopes Output

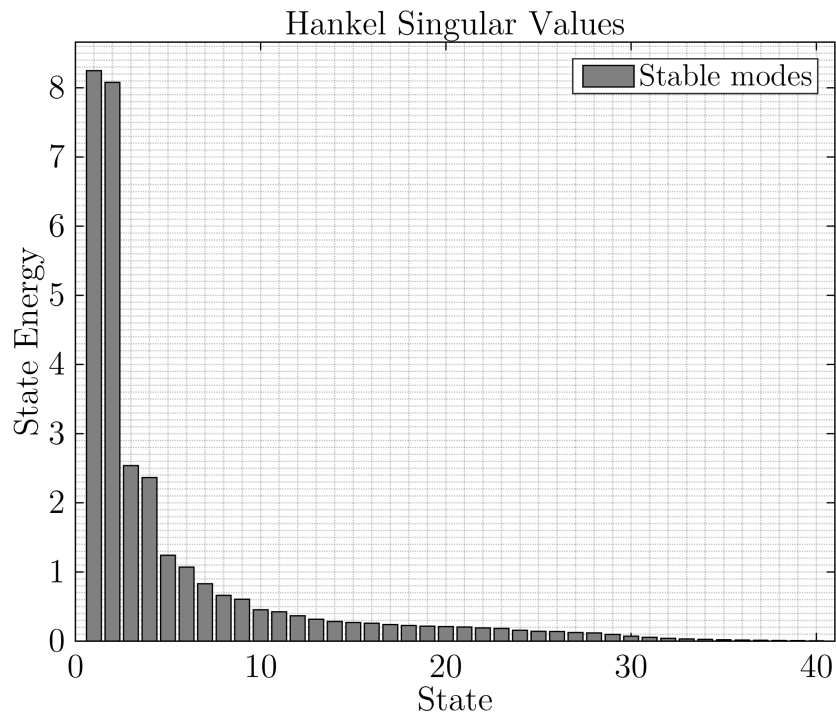


Figure 3.11: Hankel Singular Values Decomposition - Accelerometers Output

50.

It is assumed that the vibrations are mainly excited by the lateral forces generated by these two actuators. The aerodynamic forces are too distributed and weak compared to the rocket motor lateral thrust at the rear of the booster.

The only inputs to the vibration system are thus lateral forces at nodes 1 and 50. The previous system (A, B, C, D) is modified⁵ to keep only the inputs F_1 and F_{50} .

3.5.2 Sensor Placement

The state space model developed in the previous section outputs three different types of sensors : strain gages, gyroscopes and accelerometers on all possible node⁶. However, only some of these sensors need to be kept. For each of these types of sensor, the minimum number required to control the structure will be computed and the optimal locations will be determined using a technique of placement.

3.5.2.1 Placement Indices

Gawronski gives a method to quantitatively assess the location of a sensor given its type [4]. He proposes three different norms : the H_2 Norm, the H_∞ Norm and the Hankel Norm. Here, the placement will rely on H_∞ Norm. The sensors will be placed only considering the 1st bending mode. The higher modes have high natural frequencies that cannot be actively damped. Indeed Table 3.1 gives natural frequencies for the 2nd mode and higher above 25Hz which is the cutoff frequency of the actuators.

The first step is to select a set of possible locations for a type of sensor. Let be $S = \{i_1, i_2, \dots, i_s\}$ this set with s the number of possible locations. At each of these locations, an index is calculated which represents the ability of the sensor to sense the 1st bending mode at this place. This index is called σ_i for the node i . A simple way to define it is

$$\sigma_i = \|G_{1i}\|_\infty$$

where G_{1i} is the transfer function of $[F_1, F_{50}]$ to the sensor considered at node i considering only the 1st mode.

The damping ratio of the 1st bending mode is only 1% so the following approximation can be made:

$$G_{1i} \simeq \frac{\|B_1\|_2 \|C_{i1}\|_2}{2\zeta_1\omega_1}$$

The matrices B_1 and C_{i1} are the input and output matrices at node i for the sensor considered and the 1st bending mode. B_1 is the first two rows of B and C_{i1} is the first two columns of the part of C corresponding to the type of sensor considered.

⁵Only columns 1 and 50 of B and D are kept

⁶ $n - 2$ for the strain gages and n for the gyroscopes and the accelerometers

The bigger is σ_i the greater is the amplitude of the signal measured by the sensor at node i . Thanks to this method, the locations can be ranked to determine the optimal position to place the sensors. For each type of sensor - strain gages, gyroscopes and accelerometers - this technique will be used.

3.5.2.2 Strain Gages Placement

A strain gage is a long resistor fixed on the skin of the structure. When the skin is stretched or compressed, the strain gage is deformed and the electrical resistance changes. These variations of electrical resistance can be precisely measured with a Weathstone bridge. The great advantage of this sensor is its insensitivity to the rigid-body dynamics of the system. This kind of sensor measures only deformation. Thus, only one of these sensors well placed can determine the flexure of the missile. However, it will be shown later that the signal of this sensor needs to be derivated to damp the 1st mode bending. This derivation is likely to increase noise propagation. Another disadvantage is its great sensitivity to temperature variation. The booster part of the missile is greatly heated by the rocket engine and the head of the dart is aerodynamically heated. The possible locations are $x \in [2.2m, 4.4m]$ that corresponds to the set $S = \llbracket 46, 89 \rrbracket$.

The placement indices have been computed at all locations $i \in \llbracket 2, n - 1 \rrbracket$ even if the set of location is $S = \llbracket 46, 89 \rrbracket$ to show entirely how these indices vary. They appear on Figure 3.12.

On the bar plot, the placement indices of locations on the booster are very low compared to those on the dart. Indeed the booster is very stiff so it bends very few compared to the dart. The best location for a strain gage is at node 46 behind the fins at $x = 2.23 m$. This location corresponds to the strain antinode of the 1st bending mode where the flexure is maximum.

3.5.2.3 Gyroscopes Placement

A gyroscope will measure not only the pitch rate due to the vibrations but also the pitch rate of the rigid-body. For instant, at node i , a gyroscope will measure

$$q_i = q_{i,fb} + q$$

To isolate the pitch rate of the vibrations, one needs the measurements of two gyroscopes placed at different locations. Hence, the pitch rate of the rigid-body can be removed by subtraction to keep only the vibrations measurement:

$$q_i - q_j = q_{i,fb} - q_{j,fb}$$

At least two gyroscopes must be used.

A gyroscope is less sensitive to variations of temperature than a strain gage and can be placed on the booster. However a margin is kept with the two extremities of the missile because the tail is probably dense in technology because of the nozzle and

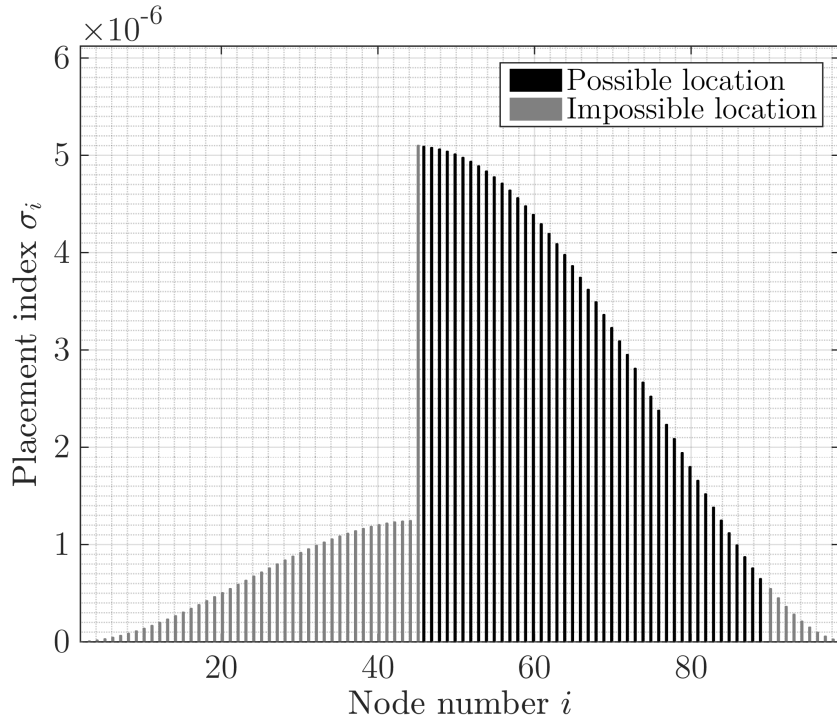


Figure 3.12: Placement Indices - Strain Gages

the nose contains a radar. For the gyroscopes, the set of locations available is then $S = [10, 92]$ corresponding to $x = [0.45m, 4.40m]$.

Figure 3.13 shows the placement indices for gyroscopes.

The nose is a place where the gyroscope would be very sensitive to the 1st bending mode. Actually, there is already a gyroscope in the sensor pack at x somewhere between 3.9 m and 4.3 m that correspond approximately to node 83. The second gyroscope must be placed at the other side of the zero pitch rate node 53. The second best position is then node 10.

3.5.2.4 Accelerometers Placement

Accelerometers measure the lateral acceleration due to vibrations but also the lateral acceleration of the rigid-body. Moreover, the acceleration on the rigid-body depends of where the sensor is placed. At node i , an accelerometer will measure:

$$a_{z,i} = a_{z,rb,CG} + (x_{CG} - x_i) \dot{q} + a_{z,fb,i}$$

thus such a measurement contains three unknowns : $a_{z,rb,CG}$, \dot{q} and $a_{z,fb,i}$. Therefore a minimum number of three accelerometers are needed at different locations to eliminate the acceleration of the center of gravity and the additional term due to pitch acceleration. This also assumes that the position of the center of gravity is accurately known, which is not correct since its position is moving during the propellant combustion.

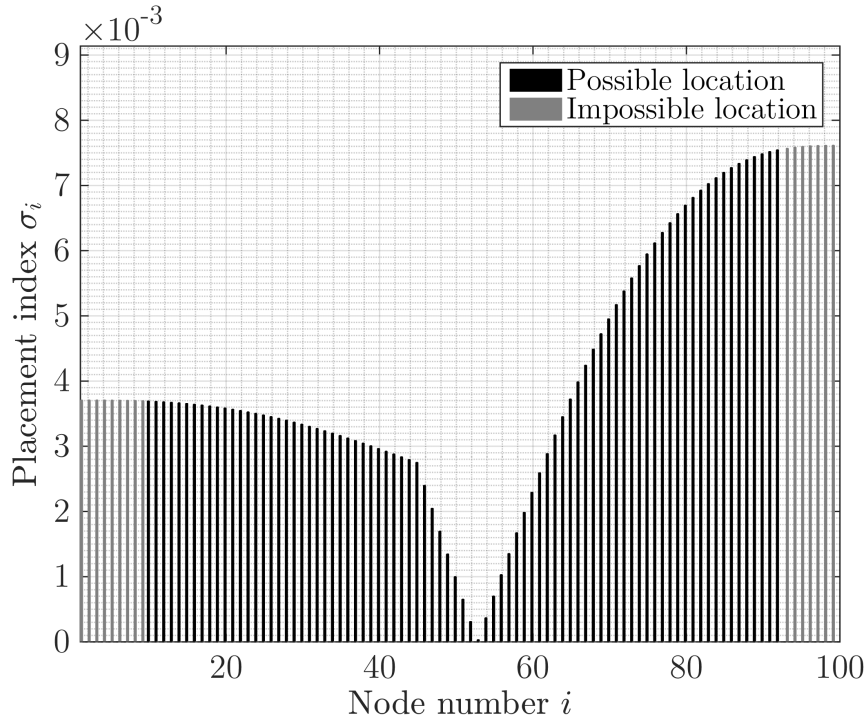


Figure 3.13: Placements Indices - Gyroscopes

Like a gyroscope, an accelerometer is not as sensible to temperature variations as a strain gage. Thus it can be placed within $x = [0.45m, 4.40m]$ corresponding to the set $S = [10, 92]$. Once again, the placement indices are calculated all over the body in Figure 3.14.

The sensor pack of the missile already contains an accelerometer along the z-axis at node 83. This position is not very sensible to the first bending mode lateral accelerations as its placement index is very low. The sensor pack seems to be placed somewhere next to the vibration acceleration node. Hence this accelerometer cannot be used for bending vibration control.

The three best locations that have a great placement index and are uncorrelated are at nodes 10, 53 and 92.

3.5.2.5 Outputs Selection

Finally, from the model established in the previous Section, only a few outputs are kept. These outputs are:

- The gyroscope and the accelerometer from the sensor pack at node 83
- The added strain gage at node 46
- The added gyroscope at node 10

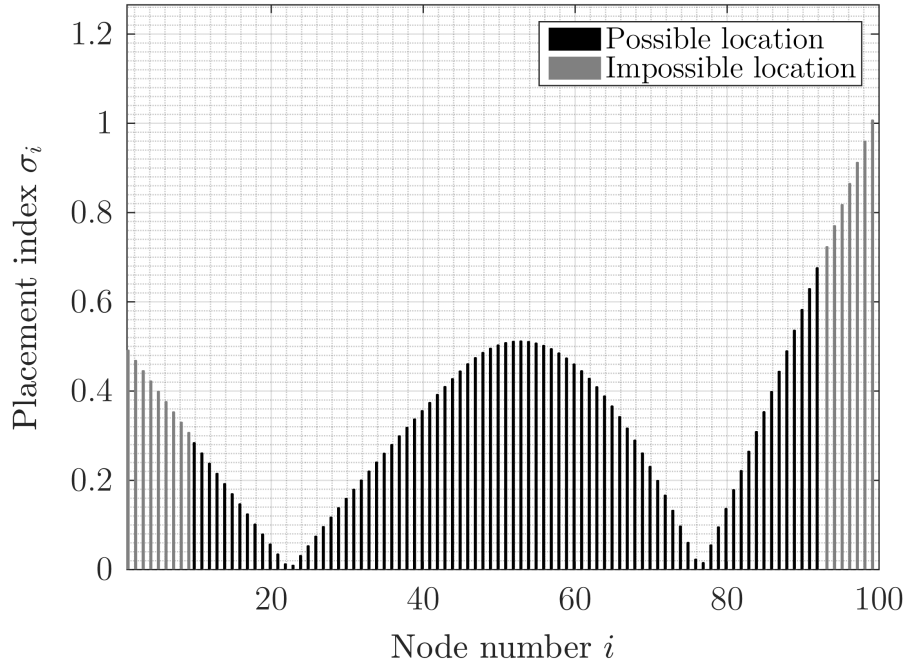


Figure 3.14: Placement Indices - Accelerometers

- The added accelerometers at nodes 10, 53 and 92

The pitch rate and acceleration outputs at node 83 will be added to the flight dynamics pitch rate and acceleration to simulate the noise created by vibrations in the inertial unit of the missile. The added strain gage at node 46, the gyroscopes at nodes 10 and 83 and the three added accelerometers at nodes 10, 53 and 92 will be used to damp the first bending mode.

All of these sensors are summarized in Figure 3.15.

3.6 Flexible Missile Model

Now that the flight dynamics and the structural model have been derived, they need to be fused into a servo-aeroelastic model where actuators, flight dynamics and structure interact. Servo-aeroelastic models can be very complicated to establish therefore assumptions will be made on the interactions between the structure and the flight dynamics. These assumptions being made, the two models will be put together and inputs and outputs will be defined.

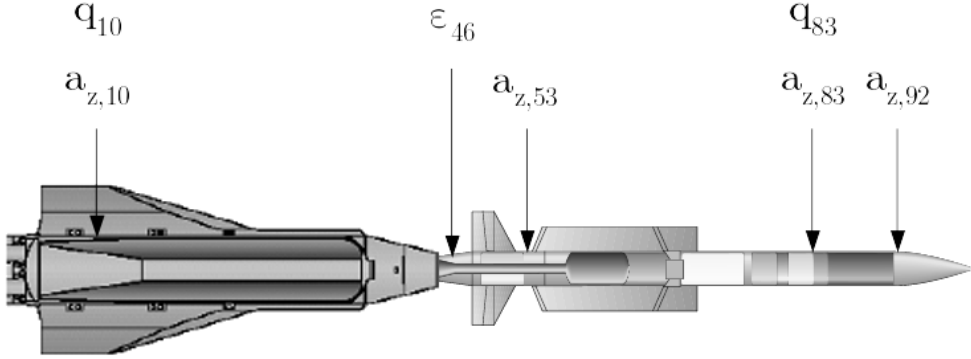


Figure 3.15: Sensors Locations - Strain gages ε , Gyroscopes q and Accelerometers a_z

3.6.1 Structural and Flight Dynamics Interactions

In Subsection 3.2.5 on page 8, it has been shown that lift and drag represent less than 10% of the efforts on the airframe. The rocket engine thrust produces the greatest force. Thus, it is assumed that the aerodynamics will not create any structural deformation. Since only bending is considered only the lateral component of the thrust is kept for the structural model input. Indeed, the longitudinal component of the thrust will create local bending moments only when the beam is bent and since the bending deflection is only about a few millimeters, this component is neglected. The lateral component of the thrust is applied at the tail, on node 1 of the structural model.

The second input to the structural model is the lateral force generated by the fins deflection. Later, the fins will be used to generate an active damping of the bending modes. The lateral force generated by these fins is inserted at node 50 of the structural model. The lift they generate is

$$L_{fins} = \frac{1}{2} \rho S V_0^2 C_{L\alpha f i n s} \delta_F$$

The lift generated by the angle of attack α is not considered since it is assumed that the body aerodynamics do not generate bending.

The inputs to the flight dynamics are the thrust vectoring and the fins deflection. These two angles are generated by second-order actuators of bandwidth of 25Hz and 50Hz before the flight dynamics block.

The last assumption is that the bending will not change the aerodynamic of the missile. Indeed the deformation is very little. The bending deflection is about a few millimeters that will not change the aerodynamic coefficients significantly. Therefore the structural model outputs will not be inputs of the flight dynamics.

3.6.2 Servo-Aeroelastic Model Inputs and Outputs

The flexible missile inputs and outputs can be classified of 5 types:

- **Control inputs:** These inputs will be used by the controller to generate a lateral acceleration or to damp the bending modes. There are two: the thrust vectoring reference orientation θ_{Tref} which commands the orientation of the nozzles with a second-order actuator and the fins reference deflection δ_{Fref} that is the input of a second-order actuator controlling the fins.
- **Sensors outputs:** There are several sensors providing information on the system. They can be accelerometers, gyroscopes or strain gages. The accelerometers and gyroscopes have a component from the flight dynamics model also called the rigid-body component and another from the structural model called the flexible-body component or vibration component. The strain gage only measures strain at node 46 from the structural model.
- **Perturbation inputs:** Some signals are perturbated by inputs. These inputs can either be sensor noise like for the accelerometers or gyroscopes or perturbation forces from the rocket engine or the fins.
- **Acceleration reference:** This input signal is generated by the navigation manager that often follow a proportional navigation. This is the reference to follow for the lateral acceleration controller.
- **Performance outputs:** They are additional outputs like the acceleration at centre of gravity, the actuators position or the vibration components of sensors that are not measured but will be used to design or assess the controllers.

This is on this model that the controllers will be designed.

Chapter 4

Active Damping Autopilots

4.1 Missile Control Inputs and Outputs

Before considering the design of the controller, an analysis must be made on the missile inputs and outputs which can be used to generate a lateral acceleration.

4.1.1 Actuators

The original ASTER-30 uses the orientatable nozzles to control the missile lateral acceleration. The nozzles are actuated with hydraulic cylinders. The thrust deflection creates a lateral force on the tail of the missile creating a pitching moment at the missile centre of gravity. This will change its angle of attack and generate a lateral acceleration. Because of the hydraulic system and the great force required to actuate the nozzles, this actuator is relatively slow. Its bandwidth is about 25Hz which is fast enough to control the lateral acceleration. The thrust vectoring will be used for the lateral acceleration control.

The thrust vectoring might be too slow for the active damping of the first bending mode. Thus, the dart fins will be used. Indeed, these fins are actuated by electric power and the efforts on these control surfaces is lower. Hence there bandwidth is about 50Hz. The first bending mode frequency is at 20Hz so the fins are fast enough to perform an active damping. Moreover, the fins deflection generate a lateral force at the missile centre. On the first bending mode shape enveloppe, this is approximatively were the lateral displacement is maximum. The fins actuator has a great influence on the first bending mode. The fins will be used to damp the bending mode.

4.1.2 Sensors

The sensors pack included in the original version of ASTER-30 contains an accelerometer and a gyroscope in the nose. These sensors are the only two needed for the lateral acceleration control. With the missile modification presented in 3.5.2 on page 31, several sensors have been added including a strain gage, gyroscopes and accelerometers.

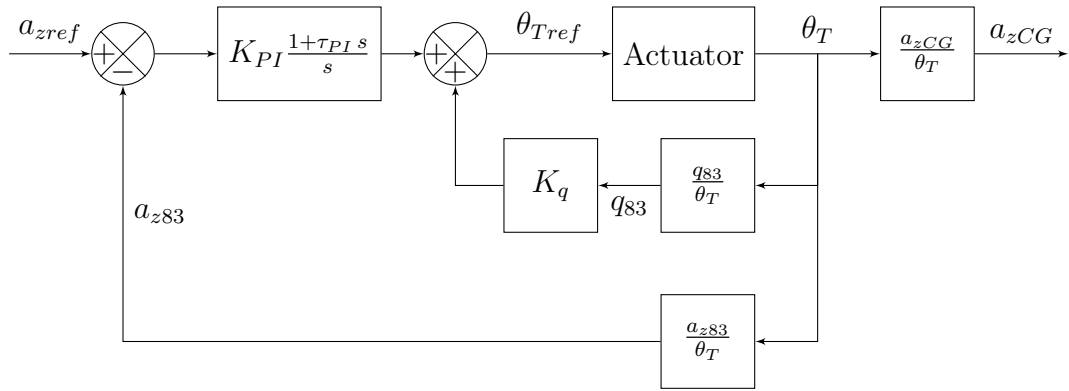


Figure 4.1: Latax Control Architecture

These additional sensors will be used for the structural active damping.

4.2 Lateral Acceleration Control

A common feedback architecture to control the lateral acceleration generation uses a pitch rate feedback plus a proportional integral controller on the lateral acceleration. In the case of a simple rigid missile, the bending is not considered. To control the lateral acceleration, the closed-loop architecture is described on Figure 4.1.

The pitch rate feedback gain K_q is chosen to damp the short period pitch oscillation (SPPO). On Figure 4.2 is shown the root locus of this feedback. It proves that the SPPO mode changes in damping ratio and very few in natural frequency. This inner loop must be as fast as possible thus a damping ratio of 0.7 might be appropriate. It yields a pitch rate feedback gain K_q of 0.022.

The proportional integral corrector on the lateral acceleration $PI(s) = K_{PI} \frac{1+0.093s}{s}$ is set to make the system as fast as possible with reasonable gain and phase margins. For instance, a good compromise is

$$PI(s) = 0.00016 \frac{1 + 0.093s}{s}$$

giving a gain margin of 18dB and a phase margin of 68deg. The proportional integral corrector will only make the SPPO natural frequency lower. Thus, this double loop architecture cannot control the lateral acceleration faster than the SPPO. The SPPO is the limit to the lateral acceleration generation.

4.3 Vibrations Alleviation

For agile missiles such as ASTER, the actuator bandwidth is very large. Thus, if the command signal generated has a non zero component at the bending frequency, the structural mode will start to oscillate. This oscillation is measured by the sensors and

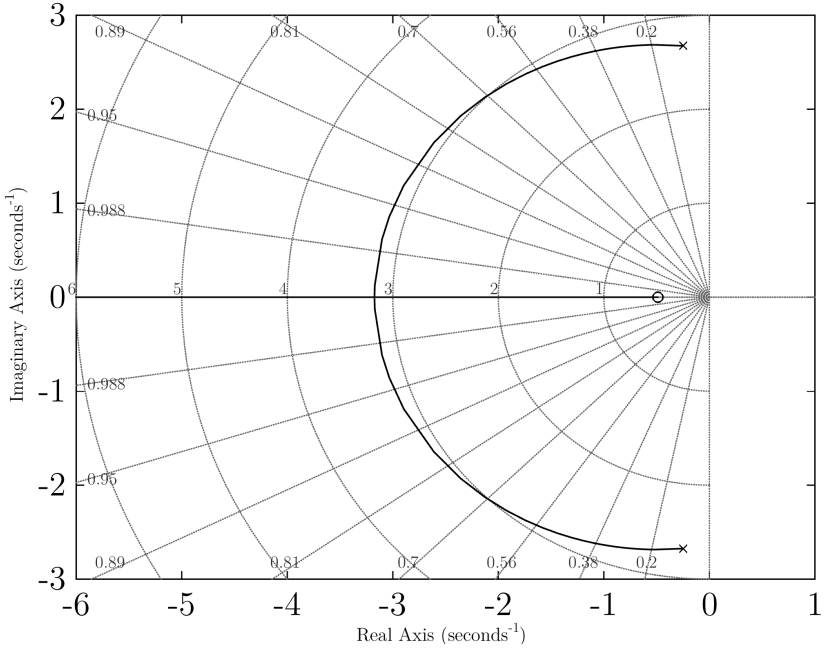


Figure 4.2: Root Locus of Pitch Rate Feedback

fed through the controller which could amplify it. On Figure 4.3 is drawn the root locus for the system open loop from the nozzle orientation reference θ_{Tref} to the pitch rate measured at the sensor pack location, on node 83 q_{83} . The 1st and the 3rd bending mode can become unstable with this feedback which is supposed to damp the shot period pitch oscillation (SPPO) if the gain is too big.

Even if the feedback gains are kept little to avoid a structural instability, the vibrations created by the rocket engine are amplified through the structure and measured by the sensors. This amplified signal will generate parasitic actuations of the thrust vectoring.

There are several strategies to deal with the bending oscillation. The first one is currently used by missile manufacturers and consists in filtering the input command to the actuator using a notch filter. This technique will be developed further in the next subsection. Now that new sensors have been added on the airframe, these measurements they provide can be used to actively damp the bending oscillations. Feedback architectures based on the strain measurement, on pitch rate measurements and on the accelerometer measurements will be investigated in the following subsections.

4.3.1 Notch Filtering

A notch filter is applied to the command of the thrust vectoring. This filter will remove any signal of the bending mode frequency. The first step is to choose the type of filter. A

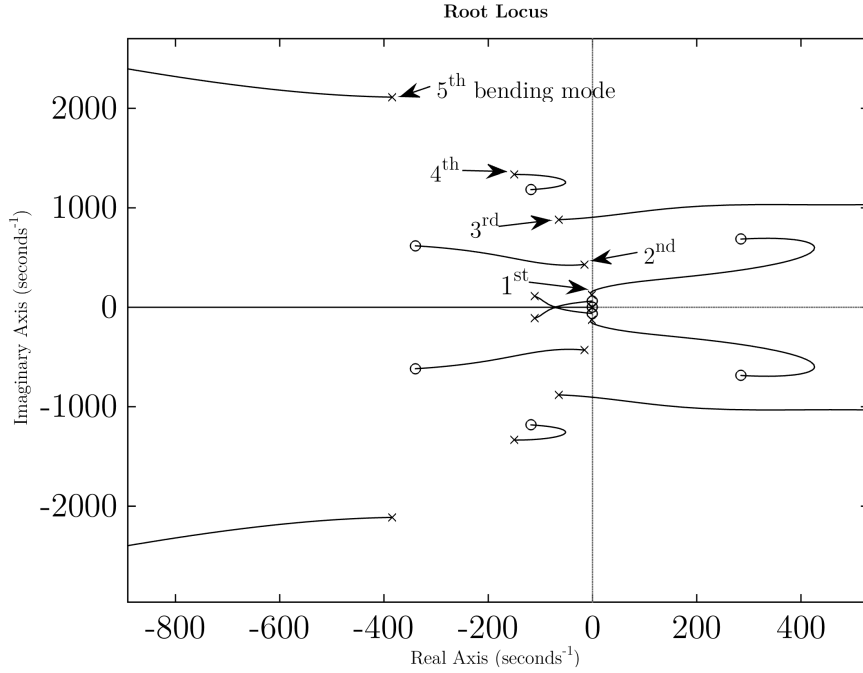


Figure 4.3: Root Locus of $\frac{q_{83}}{\theta_{Tref}}$

Chebyshev Type II filter suits the problem because there is no ripple in the bandwidth that could create gain distortion and affect performance at low frequency. However, this type of filter requires a high order denominator to ensure a sharp gain loss. The filter center frequency is set to 20Hz with a stopband bandwidth of $\pm 10\%$. Indeed, the uncertainty on the first bending mode frequency is about $\pm 10\%$. The gain loss is set to 20dB. The order of the filter is 4. With these criterias, the corresponding Chebyshev Type II filter is

$$N(s) = \frac{s^4 + (3.55 \cdot 10^{-15}) s^3 + (3.19 \cdot 10^4) s^2 + (1.71 \cdot 10^{-10}) s + 2.49 \cdot 10^8}{s^4 + 72.0 s^3 + (3.45 \cdot 10^4) s^2 + (1.14 \cdot 10^6) s + 2.49 \cdot 10^8}$$

The Bode diagram of the filter is plotted on Figure 4.4. The phase loss brought by this notch filter is already -30° at 70 rad.s^{-1} that may bring poorer performance even at low frequencies.

Thanks to this filter, the actuator will excite less the first bending mode. The bode diagram of $\frac{q_{83}(s)}{\theta_{Tref}(s)}$ is plotted on Figure 4.5. This shows clearly that the resonance peak of the first bending mode has been cut down by 20dB.

Once the filter is plugged to the system input, a conventional pitch rate feedback with a proportional integral controller on the acceleration can be designed. The new feedback architecture is drawn on Figure 4.7.

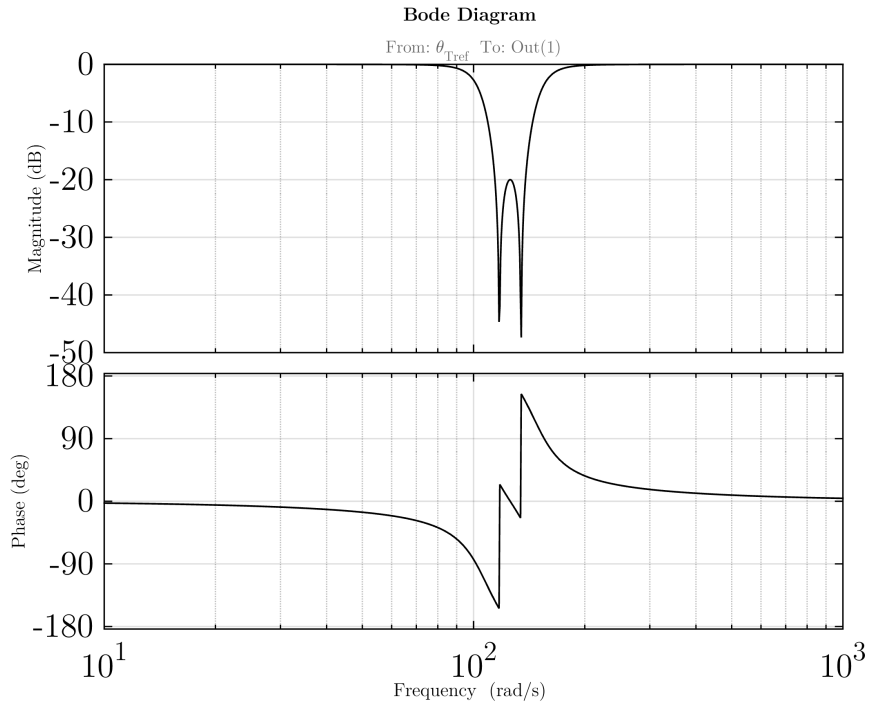
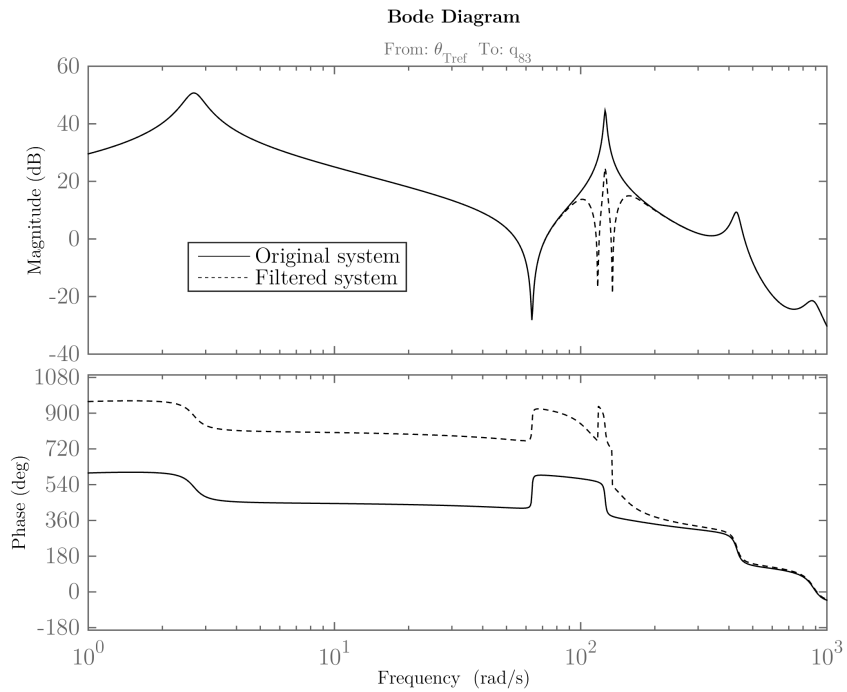


Figure 4.4: Bode Diagram of the Notch Filter


 Figure 4.5: Bode Diagram of $\frac{q_{83}(s)}{\theta_{T\text{ref}}(s)}$

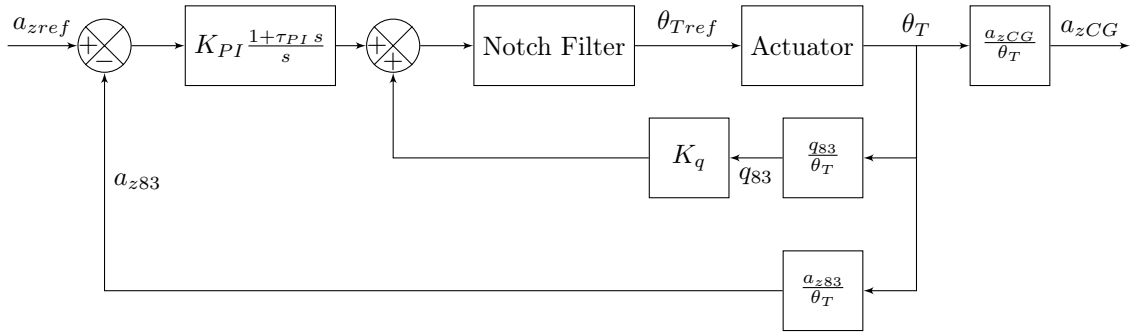


Figure 4.6: Closed-Loop with Notch Filter

Figure 4.7: Closed-Loop with Notch Filter

4.3.2 Active Structural Damping

The notch filter is a simple solution to deal with vibrations but it does not remove them. Another way to overcome bending oscillations is to artificially augment the damping ratio of the bending mode. This is called active structural damping.

4.3.2.1 Requirements

The controller must generate a force that is opposite to the vibration speed to damp the bending oscillations. To do so, the controller can either use the thrust vectoring or the central fins. The natural frequency of the first mode is 20Hz. The bandwidth of the thrust vectoring is about 25Hz which is too low: at 20Hz, the thrust vectoring actuator has a phase loss of -70° and a gain loss of -1.5dB as shown on Figure 4.8. This is very close to the cutoff frequency and the real behaviour of the actuator at this frequency is not accurately modeled.

The fins have a bandwidth of 50Hz that is more than the double of the bending mode frequency. The phase loss at 20Hz is only -34° and the gain loss is -0.1dB as shown on Figure 4.9. Therefore this fast actuator is to be preferred for active damping of the first bending mode.

4.3.2.2 Strain Feedback

The strain gage is a sensor that is usually not present on a missile airframe. With this extra sensor, it is possible to measure the local strain on the skin of the structure to infer on its flexure. This additional information can help to deal with bending oscillation. It has been chosen to damp the first bending mode oscillation with the central fins. At the bending mode frequency, the fins deflection have very little influence on the slow rigid-body dynamics. Moreover, they are located close to the center of gravity so they do not create a big change in the angle of attack. If only the first bending mode is considered, the transfer function of the fins deflection to the strain can be approximated

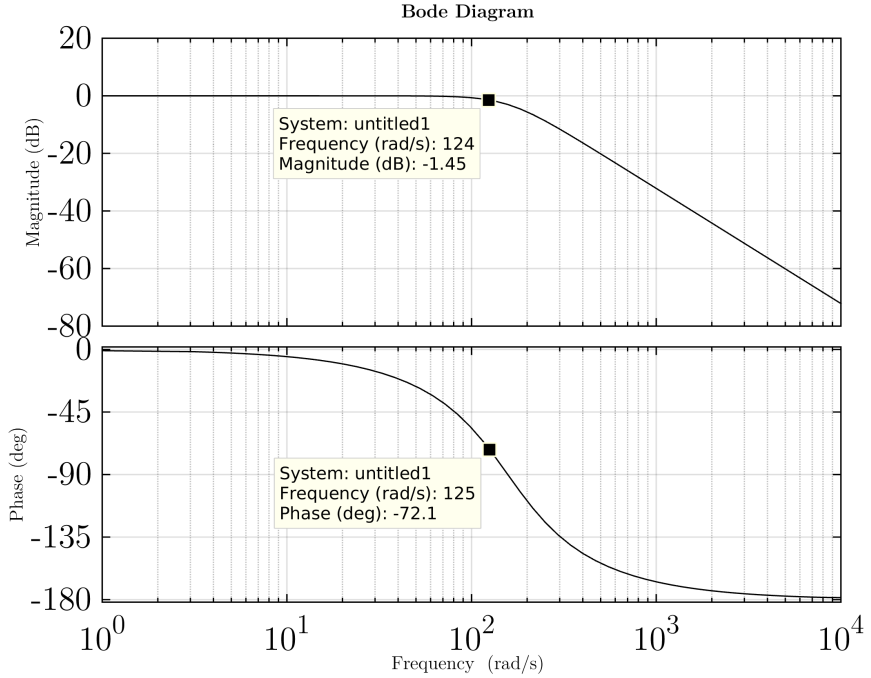


Figure 4.8: Bode Diagram of $\frac{\theta_T(s)}{\theta_{Tref}(s)}$

to:

$$\frac{\varepsilon_{46}}{\delta_F}(s) = K_{\varepsilon/\delta_F} \frac{\omega_1^2}{s^2 + 2\zeta_1\omega_1 s + \omega_1^2}$$

To increase the term ζ_1 with a simple feedback, the strain measurement needs to be derived as shown in the block diagram in Figure 4.10. The transfer function of the closed-loop would then be

$$\frac{\varepsilon_{46}}{\delta_F CL}(s) = K_{\varepsilon/\delta_F} \frac{\omega_1^2}{s^2 + 2(\zeta_1 + K_{\varepsilon/\delta_F}\omega_1 K)\omega_1 s + \omega_1^2}$$

The feedback gain K directly changes the damping ratio of the first bending mode without changing the static gain K_{ε/δ_F} or the natural frequency ω_1 . However this feedback is non causal and a pole needs to be added. This artificial pole can be placed very fast to minimize its influence on the dynamics. The feedback transfer function would then be

$$K \frac{s}{1 + s/\omega_{fast}}$$

This feedback loop would work if the fins deflection dynamics were very fast. This is not the case because even if there bandwith is twice bigger than the bending mode natural frequency, the phase loss is non negligible.

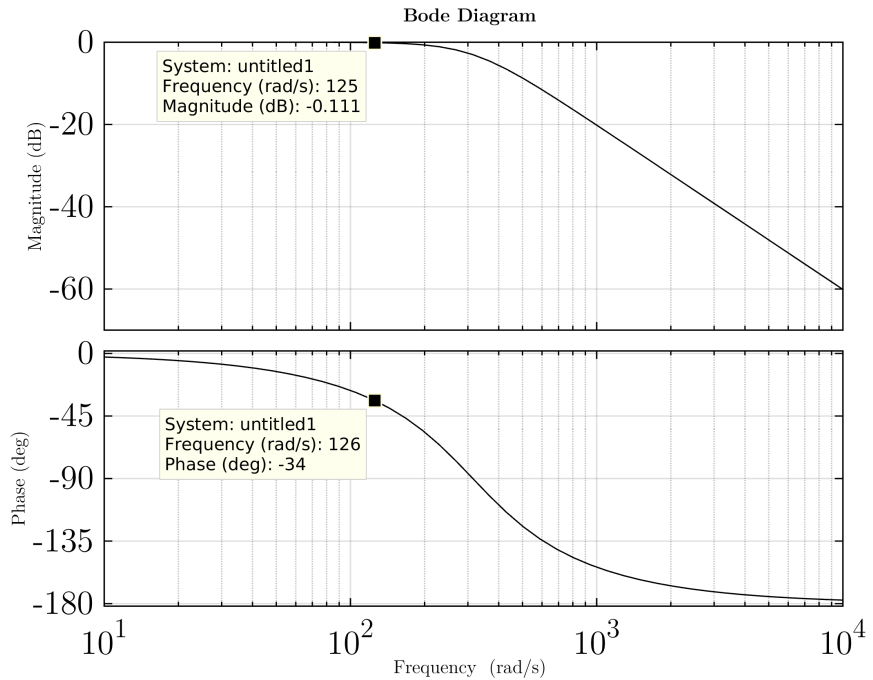


Figure 4.9: Bode Diagram of $\frac{\delta_F(s)}{\delta_{Fref}(s)}$

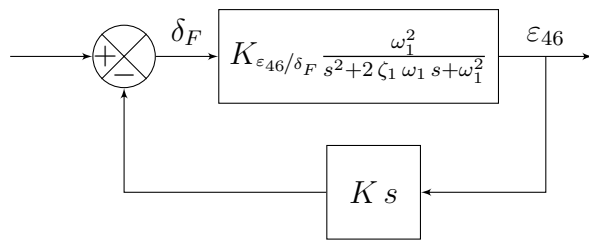


Figure 4.10: Block Diagram of Derivative Strain Feedback

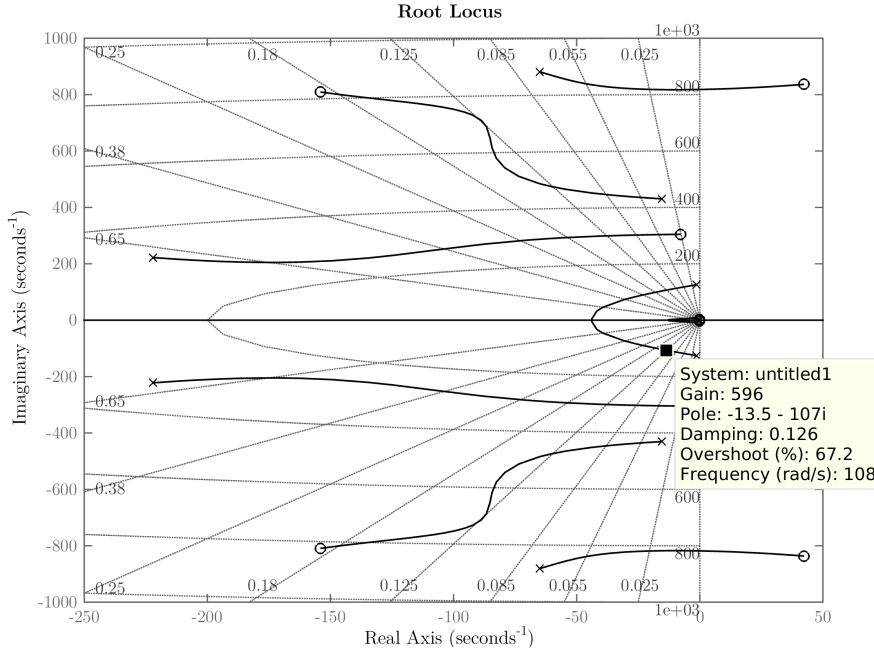


Figure 4.11: Root Locus of $\frac{\varepsilon_{46}}{\delta_{Fref}}(s)$

Fortunately, this phase shift acts slightly like a differentiator and a simple proportional feedback will damp the bending oscillations. On Figure 4.11, a root locus has been plotted with the full dynamics of all 5 bending modes, flight dynamics and actuator dynamics. With a proportional feedback gain of 600, the damping ratio of the first bending mode has been increased by 10 to 12.5%. This gain is chosen to obtain a gain margin of 6dB and a phase margin of 30°.

With this first loop, the bode diagram of $\frac{q_{83}}{\theta_{Tref}}(s)$ on Figure 4.12 shows that the first bending mode is clearly damped. The resonance peak at 125 rad.s^{-1} has been cut down thoroughly.

This active damping replaces the notch filter seen in 4.3.1 on page 40. The complete feedback architecture containing the strain feedback, the pitch rate loop and the proportional integrator corrector is on Figure 4.13.

This feedback architecture has some disadvantages though. The strain measured is not only coming from bending deformations. Some longitudinal or twisting modes may create local strains and propagate noise in the system. Moreover, the static bending will create a static deflection of the fins and increase drag.

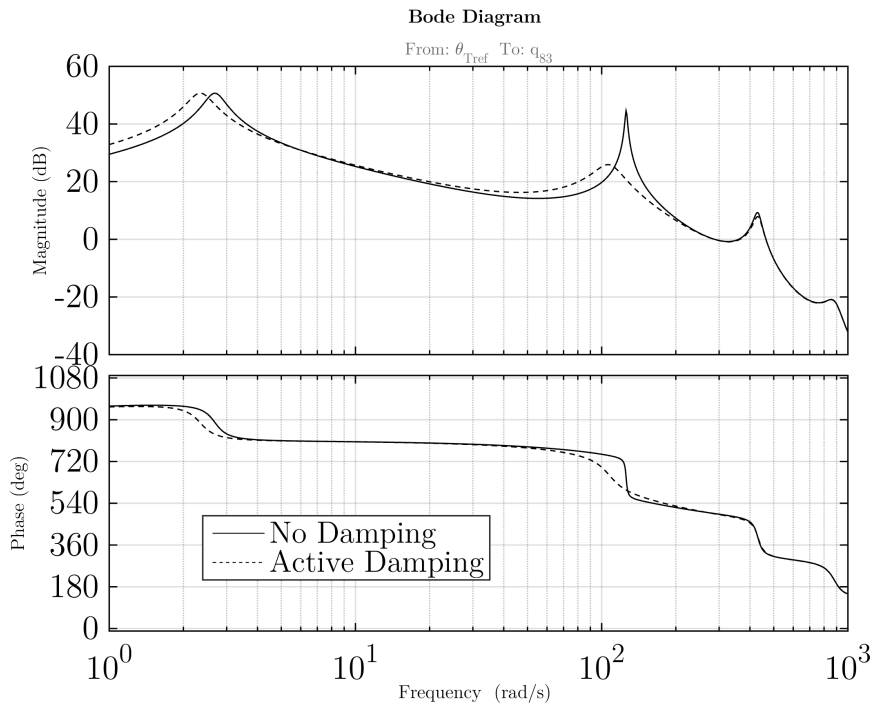


Figure 4.12: Bode of $\frac{q_{83}}{\theta_{Tref}}(s)$ With and Without Strain Feedback

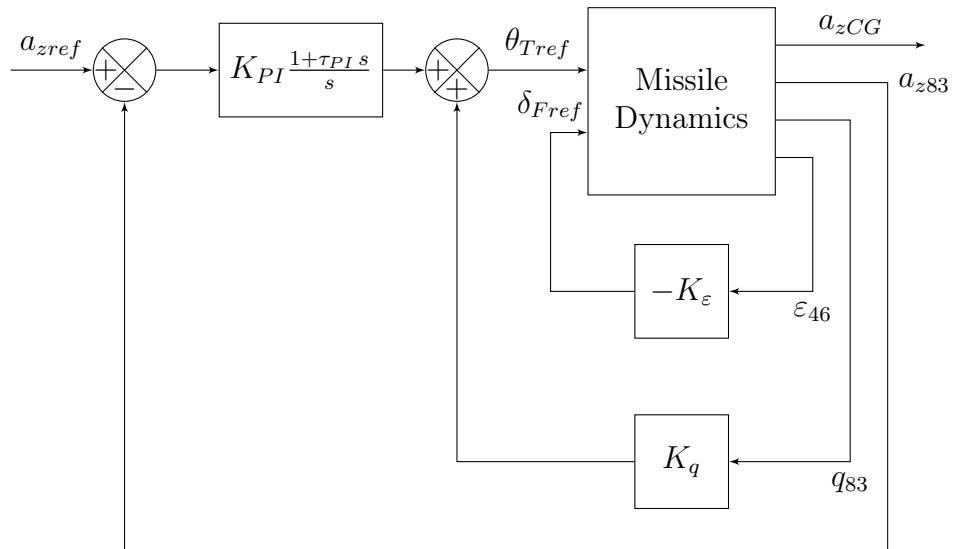


Figure 4.13: Feedback Architecture with Strain Gages

4.3.2.3 Gyroscope Feedback

Two gyroscopes can give information on the flexure. A gyroscope is placed at the rear and the other one is the gyroscope included in the sensor pack next to the nose. The problem with damping bending with gyroscopes is that they measure not only the local pitch rate of the bending but also the rigid-body pitch rate. Thus two of them are needed to subtract the rigid-body pitch rate. Indeed, a gyro at node i will measure $q_i = q_{RB} + q_{FBi}$. The subtraction of the signals coming from the two gyroscopes will give:

$$q_{10} - q_{83} = q_{FB10} - q_{FB83} = \Delta q$$

If only the first bending mode is considered, the transfer function of the fins deflection δ_F to the pitch rate difference Δq_{FB} is

$$\frac{\Delta q}{\delta_F}(s) = K_{\Delta q/\delta_F} \frac{\omega_1^2 s}{s^2 + 2\zeta_1 \omega_1 s + \omega_1^2}$$

thus with a simple proportional feedback gain $K_{\Delta q}$ from Δq_{FB} to δ_F would change modify the transfer function to

$$\frac{\Delta q}{\delta_F}_{CL}(s) = K_{\Delta q/\delta_F} \frac{\omega_1^2 s}{s^2 + 2(\zeta_1 + K_{\Delta q/\delta_F} \omega_1 K_{\Delta q}) \omega_1 s + \omega_1^2}$$

This feedback would damp the first bending mode without modifying the other parameters. Now considering the phase loss of the actuator of about 30° , the natural frequency of the first bending mode will change but damping is still possible. On Figure 4.14 the root locus of $\frac{\Delta q}{\delta_{Fref}}(s)$ shows that a damping of 12% on the first bending mode can be achieved with a feedback gain $K_{\Delta q} = 0.24$.

The effect of this loop on the resonance peak of the first bending mode can be seen on Figure 4.15. The resonance peak is reduced.

To this damping loop are added the conventional feedbacks on the pitch rate and the lateral acceleration. The complete architecture in this case is draw on Figure 4.16.

This controller architecture has the disadvantage that the two gyroscopes must be similarly calibrated and synchronized to perform the subtraction correctly. The great advantage is the absence of fins deflection in static.

4.3.2.4 Accelerometer Feedback

Using accelerometers for the feedback is more complicated than using gyroscopes. At node i , the accelerometer will measure $a_{z,i} = a_{z,CG} + (x_{CG} - x_i) \dot{q} + a_{zi,fb}$. There are three unknowns in this equality: $a_{z,CG}$, \dot{q} , and $a_{zi,fb}$ hence three uncorrelated accelerometers are needed to keep only the flexible body component. On the airframe, three accelerometers have been added at node 10, 53 and 92. Considering only the first bending mode,

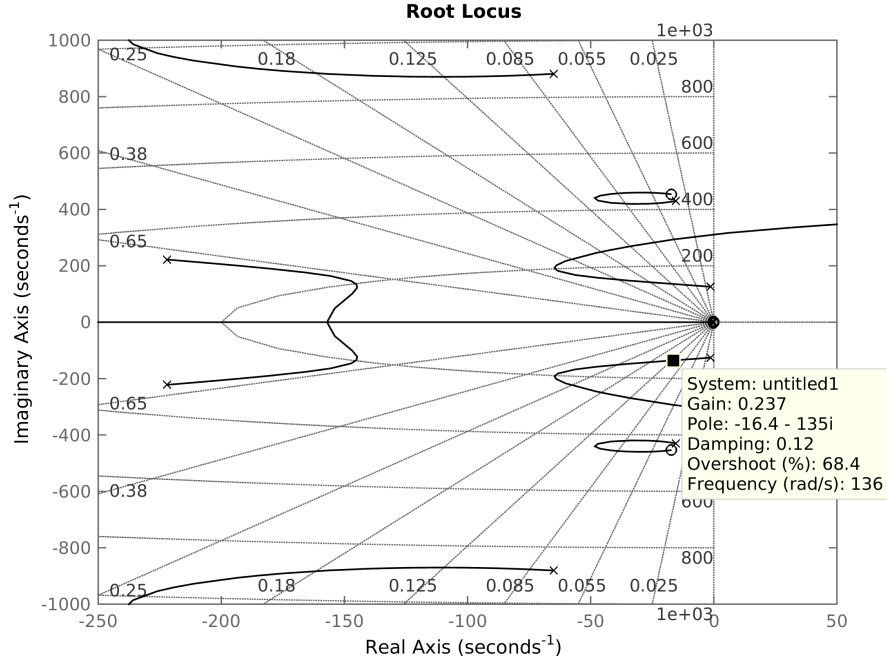


Figure 4.14: Root Locus of $\frac{\Delta q}{\delta_{Fref}}(s)$

all the $a_{zi,fb}$ are proportional to the first bending mode mean acceleration $a_{z,m1}$. A linear combination of these three measurements must be found so that it does not depend of $a_{z,CG}$ and \dot{q} . Let (c_{10}, c_{53}, c_{92}) be three coefficients so that

$$c_{10}a_{z,10} + c_{53}a_{z,53} + c_{92}a_{z,92} = c a_{z,m1}$$

where c is a non zero real number. Let say that $c_{10} = 1$ to make the linear system of Cramer. In a matrix form, this gives

$$\begin{bmatrix} 1 & 1 & 1 \\ 9 & 52 & 91 \\ 1 & 0 & 0 \end{bmatrix} \begin{bmatrix} c_{10} \\ c_{53} \\ c_{92} \end{bmatrix} = \begin{bmatrix} 0 \\ 0 \\ 1 \end{bmatrix}$$

The solution is $\begin{bmatrix} c_{10} \\ c_{53} \\ c_{92} \end{bmatrix} = \begin{bmatrix} 1 \\ -82/39 \\ 43/39 \end{bmatrix}$. The linear combination $c_{10}a_{z,10} + c_{53}a_{z,53} + c_{92}a_{z,92}$ will be called $\sum a_z$.

The transfer function of the fins deflection to this linear combination of accelerations is of the form

$$\frac{\sum a_z}{\delta_F}(s) = K_{\sum a_z/\delta_F} \frac{\omega_1^2 s^2}{s^2 + 2 \zeta_1 \omega_1 s + \omega_1^2}$$

hence to damp the first bending mode, the feedback needs an integrator so that the resulting transfer function would be

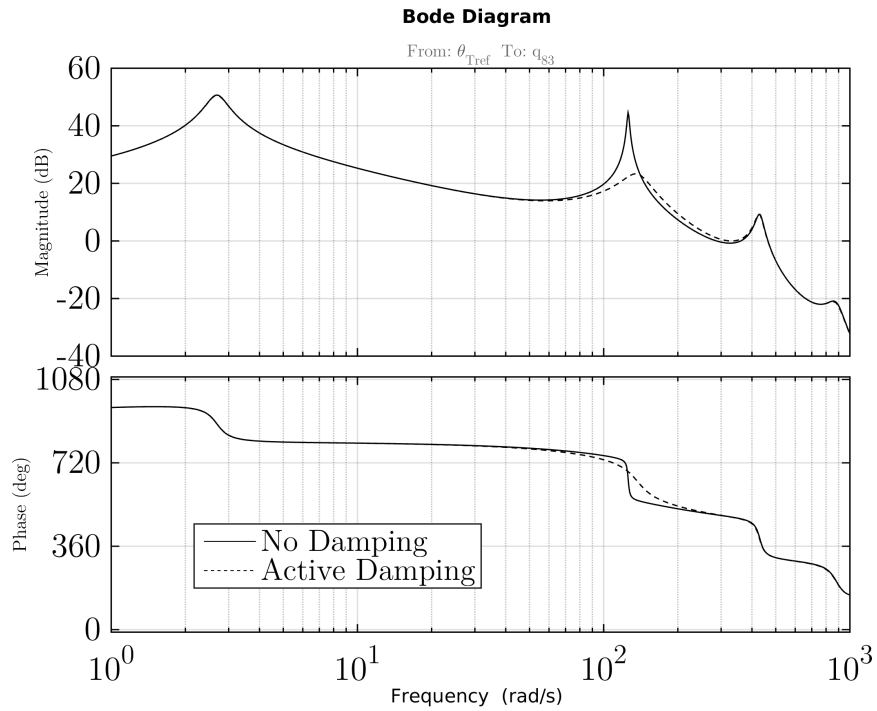


Figure 4.15: Bode of $\frac{q_{83}}{\theta_{Tref}}(s)$ With and Without Δq Feedback

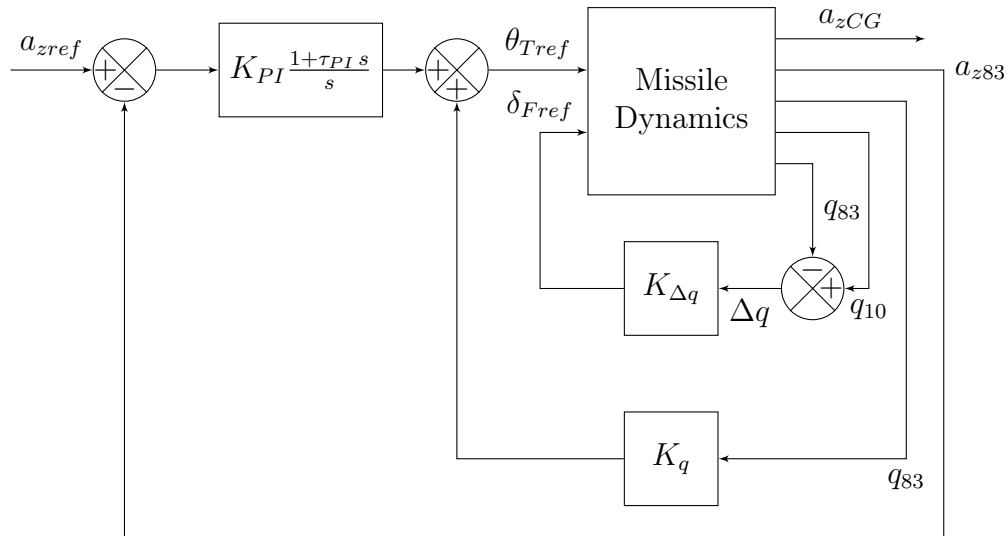


Figure 4.16: Feedback Architecture with Gyroscopes

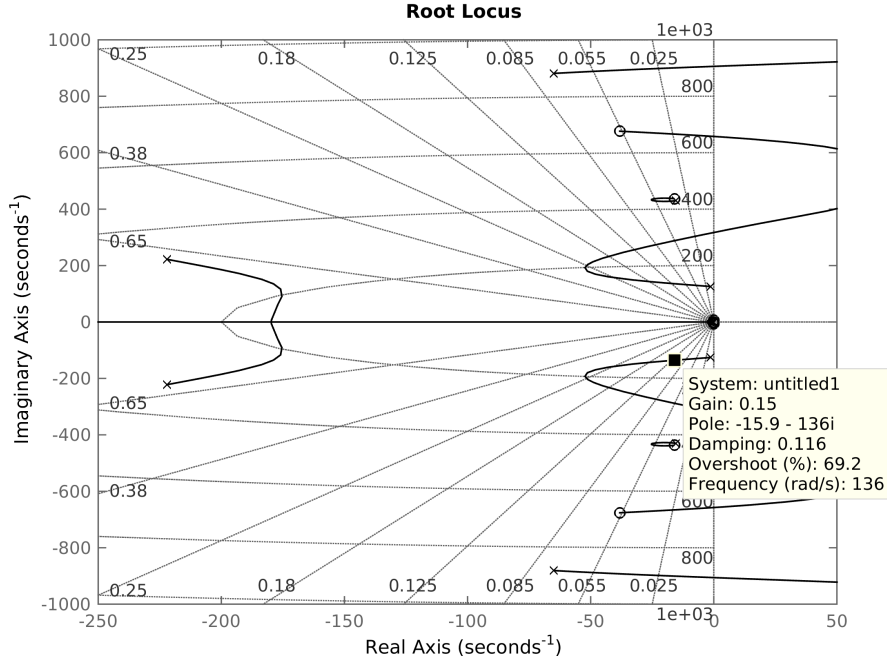


Figure 4.17: Root Locus of $\frac{\Delta q}{\delta_{Fref}}(s)$

$$\frac{\sum a_z}{\delta_F}_{CL}(s) = K_{\sum a_z/\delta_F} \frac{\omega_1^2 s^2}{s^2 + 2(\zeta_1 + K_{\sum a_z/\delta_F} \omega_1 K_{a_z}) \omega_1 s + \omega_1^2}$$

Like for the gyroscopes, the phase loss of the fins actuator will generate a change in the bending oscillation natural frequency. The root locus of $\frac{1}{s} \frac{\sum a_z}{\delta_F}$ is plotted on Figure 4.17 and shows that the first bending mode can be damped to 12% with a gain K_{a_z} of 0.16.

A comparative Bode plot shows on Figure 4.18 the effect of such a damping architecture. Once again the resonance peak has been cut off.

The complete controller architecture is drawn in Figure 4.19.

Using accelerometers for structural damping might bring some problems because the accelerometers must be similarly calibrated and synchronized like the gyroscopes. The position of the center of gravity does not need to be known. Indeed when the linear equation system has been solved, the solution do not depend on the center of gravity abscissa.

4.4 H_∞ Fixed-Structure Tuning

Five controller architectures will be assessed. They all have in common the lateral acceleration control composed of a pitch rate feedback and a proportional integral

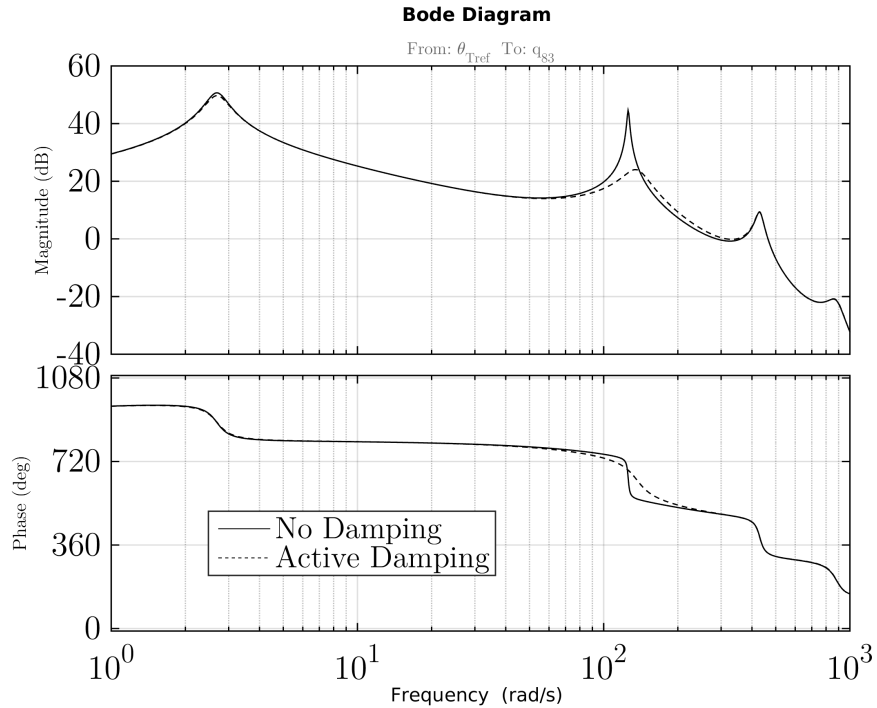


Figure 4.18: Bode of $\frac{q_{83}}{\theta_{Tref}}(s)$ With and Without $\sum a_z$ Feedback

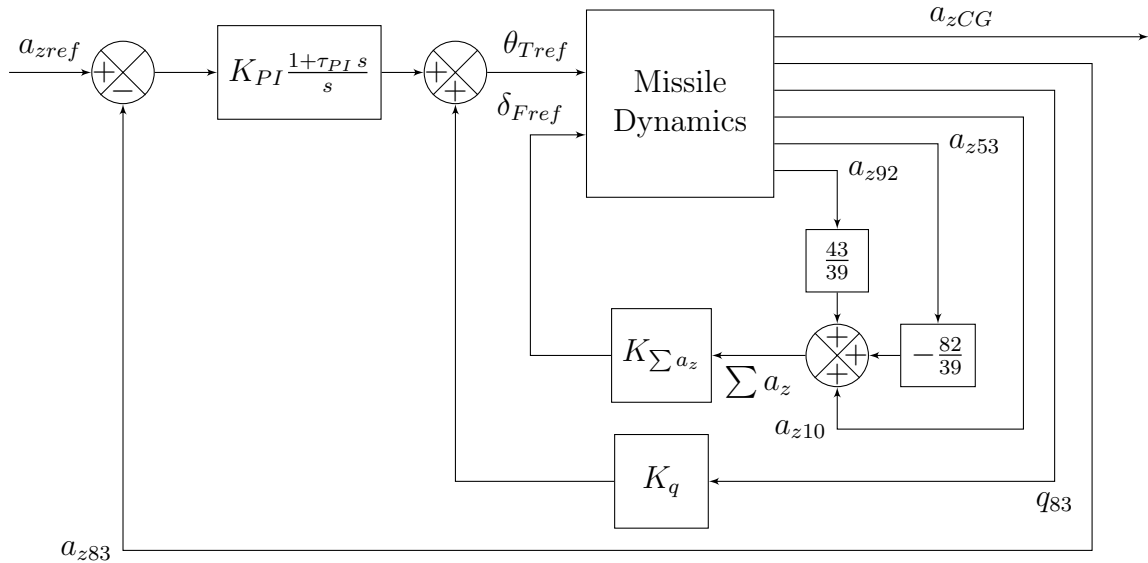


Figure 4.19: Feedback Architecture with Accelerometers

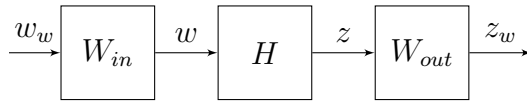


Figure 4.20: Weighted Form for H_∞ -tuning

controller on the lateral acceleration. The first architecture will have no additional feature, the second one has a notch filter. The controller number 3 to 5 use active damping using respectively:

- the strain gage feedback,
- the 2 gyroscopes feedback,
- the 3 accelerometers feedback.

These architectures will be tuned using the same criterias to eventually compare their performance. The method will use the H_∞ -tuning for fixed-structure controllers developped by P. Apkarian in [1].

Each architecture is put in a weighted form like on Figure 4.20. The input to the closed-loop system is the exogenous vector w which contains all the input having requirements. The output is the performance vector z containing all the performance indices that one will minimize. The diagonal matrices W_{in} and W_{out} are weights applied to w and z to define the requirements. The algorithm will tune the controller gains in order to make the system stable while minimizing γ such that

$$\|W_{out}HW_{in}\|_\infty < \gamma$$

The parameters subject to tuning are K_q , K_{PI} and τ_{PI} . The notch filter, the strain feedback, the gyroscopes feedback or the accelerometers feedback are not tunable. They are defined in 4.3 on page 39.

The exogenous vector w only contains the reference lateral acceleration a_{zref} . The corresponding weight is set to 1. Thus, the other signals weights will be chosen for a reference acceleration of 1m.s^{-1} . Additional inputs are not needed. First of all because the tuning needs to be simply made but also because other inputs like noise, actuators perturbations or gust perturbations are neglected. The sensors noise is very low compared to signals generated by vibrations. The fins actuator perturbations is assumed to be very few compared to the thrust vectoring perturbations which will not be considered for tuning but later for assessment. Finally, gusts have a speed which is negligible compared to the missile speed of Mach 2.

The performance vector z is composed of two signals: the lateral acceleration error $a_{zref} - a_{zCG}$ and the thrust vectoring orientation θ_T . It is obvious that the lateral acceleration error is needed in z to design a lateral acceleration controller. The thrust vectoring orientation θ_T is added in z to limitate the use of this actuator which has

Controller number	$K_q(s)$	K_{PI} (rad·s/m)	$\tau_{PI}(s)$
1	$1.69 \cdot 10^{-2}$	$3.96 \cdot 10^{-5}$	0.140
2	$1.69 \cdot 10^{-2}$	$23.0 \cdot 10^{-5}$	0.140
3	$2.02 \cdot 10^{-2}$	$27.3 \cdot 10^{-5}$	0.122
4	$1.69 \cdot 10^{-2}$	$23.0 \cdot 10^{-5}$	0.140
5	$1.60 \cdot 10^{-2}$	$23.0 \cdot 10^{-5}$	0.141

 Table 4.1: H_∞ -tuned Controllers Parameters

a rate limit, a deflection limit and second-order dynamics. The output weight matrix W_{out} is then

$$\begin{bmatrix} W_{err} & 0 \\ 0 & W_{\theta_T} \end{bmatrix}$$

W_{err} is set to minimize the error at low frequency and bound it at high frequency for resonance reduction. The controller is equipped with an integrator so the error will tend to 0. An empirical tuning of this weight is

$$W_{err}(s) = \frac{1.5}{s}$$

which will force the bandwidth to be 1.5 rad/s. The target shape of $H_{a_{zref} \rightarrow a_{zref} - a_{zCG}}(s)$ will be the inverse of $W_{err}(s)$.

W_{θ_T} is chosen to avoid using the actuator over its cutoff frequency. A simple way to do this is to choose

$$W_{\theta_T}(s) = 1/5 \cdot 10^{-3} \left(\frac{\omega_T}{s}\right)^2$$

where ω_T is the actuator cutoff frequency of 25Hz (157 rad/s). The coefficient $5 \cdot 10^{-3}$ is empirically set. Once again, the target shape of $H_{a_{zref} \rightarrow \theta_T}(s)$ is $1/W_{\theta_T}(s)$. The rotation speed of the thrust vectoring must also be bounded. The system being represented as linear, trying to minimize $\dot{\theta}_T$ will also minimize $\ddot{\theta}_T$. The corresponding bound will be s/W_{θ_T} .

The H_∞ -tuning yields parameters summarized in Table 4.1. The algorithm found a minimum γ between 1.01 and 1.04 for all of them. The controller number 1 has no vibration alleviation device and the closed-loop will be named “Raw”. The controller number 2 utilizes a notch filter so will be called “Notch”. The controllers 3, 4 and 5 actively damping vibrations with:

- (3) a strain gage,
- (4) 2 gyroscopes,
- (5) 3 accelerometers.

These 3 last closed-loop will be called “Strain”, “Gyro”, and “Acc”.

These settings are very similar especially for controllers alleviating vibrations. These controllers will be assessed and compared in the Section 4.5.

4.5 Controllers Assessment and Comparison

4.5.1 Robustness to Uncertainty

The first criteria to assess is robustness to uncertainty. The H_∞ algorithm has found stable solutions for the five architectures but they can turn unstable with some parameters variation.

The uncertainty has been derived considering the thrust, the center of gravity, the bending modes natural frequencies and their damping ratios as uncertain parameters. To assess robustness, gain margin and phase margin are of little help for such a MIMO system. Each uncertain system is an infinite set of possible realization. A finite subset of systems are created from this uncertain system and their poles are plotted on Figure 4.21. The poles keep a reasonable margin with the imaginary axis. These closed-loop system are robust to the designed uncertainty.

4.5.2 Tracking

The tracking performance of these 5 closed-loop is their ability to generate a lateral acceleration equal to the reference acceleration. Step responses give a good insight to assess the tracking performance. These responses are plotted on Figure 4.22.

Another index for tracking performance is the singular values of the transfer function from the reference acceleration a_{zref} and the error $a_{zref} - a_{zCG}$ which is on Figure 4.23.

Looking at these two figures, the five different closed-loop architectures yield very similar tracking performance. The rise time from 10 to 90% following a step demand is between 0.741 and 0.765s and the 2% settling time is between 4 and 4.13 s. These responses are rather slow for a missile but the double loop architecture presented cannot create dynamics faster than the SPPO. Moreover, during the acceleration phase, ASTER-30 does not need to be highly manoeuvrable. A high manoeuvrability would be required during the target tracking phase. The sigma plots provide information about tracking performance over all frequencies. The presence of an integrator in the loop gives makes the error converge to zero at low frequencies. The bandwidth at -3dB is between 1.09 and 1.17 rad.s^{-1} .

4.5.3 Actuators Demand

The thrust nozzles cylinders and the fins actuators have second order dynamics and actuators demand must be limited at high frequency. These demands must also be limited over the whole range of frequencies to save energy and to avoid actuators heating and damage.

4.5.3.1 Demand for Lateral Acceleration

The actuators demand following a lateral acceleration command must be appropriately bounded. The weight W_{θ_T} ensures that the position and rate of the thrust vectoring

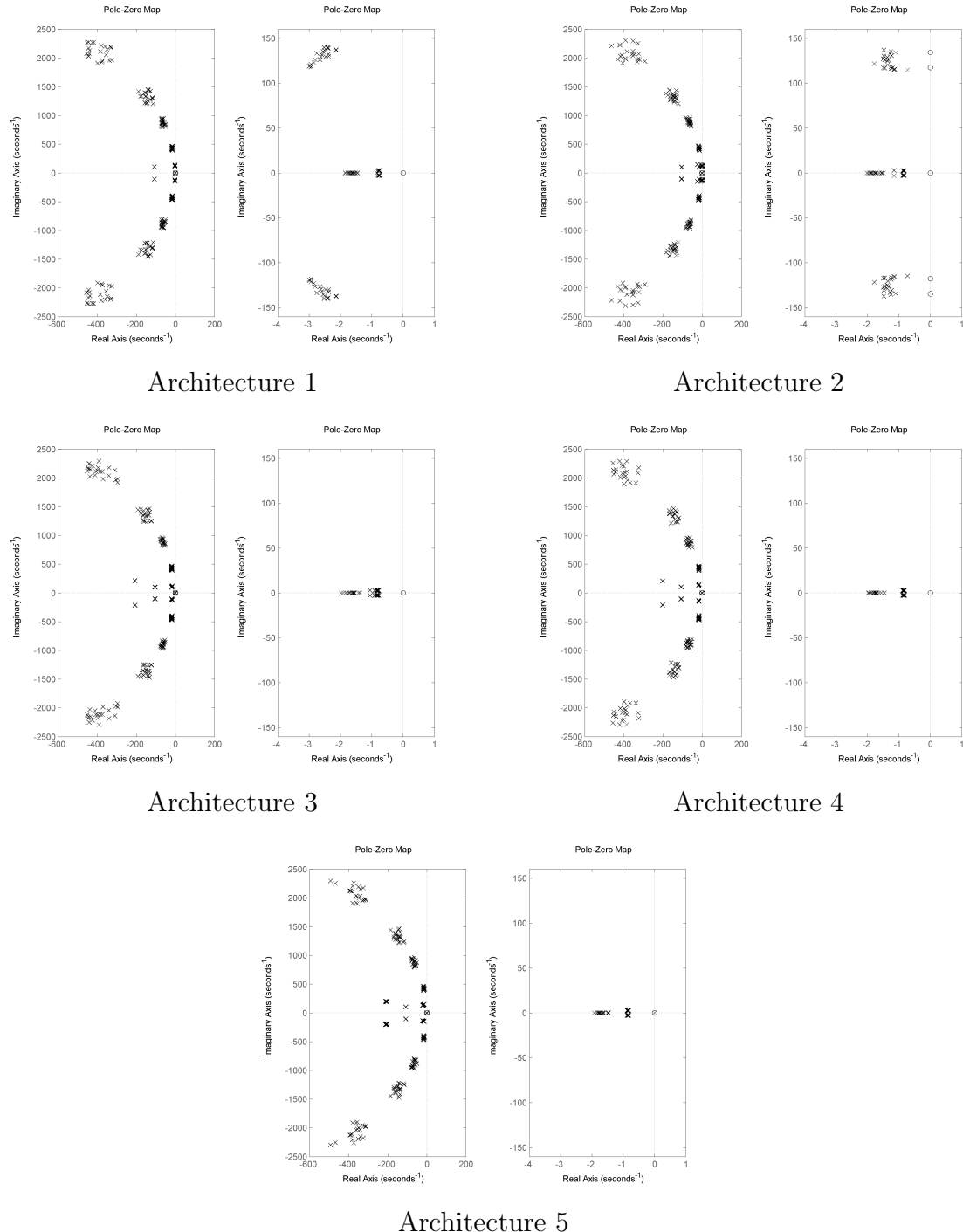


Figure 4.21: Poles of Closed Loop 1 to 5 Subject to Uncertainty

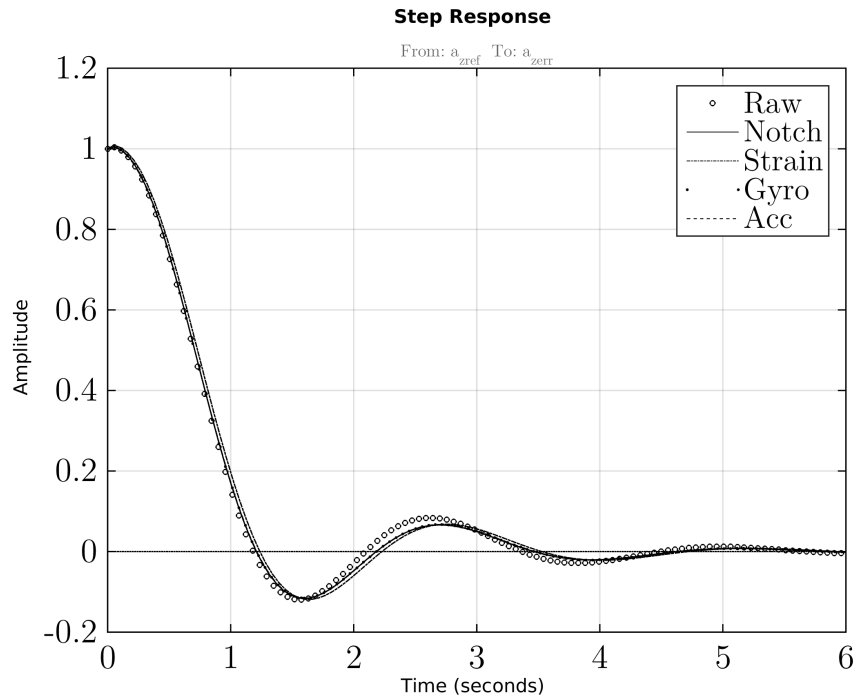


Figure 4.22: Step Response of a_{zref} to $(a_{zref} - a_{zCG})$

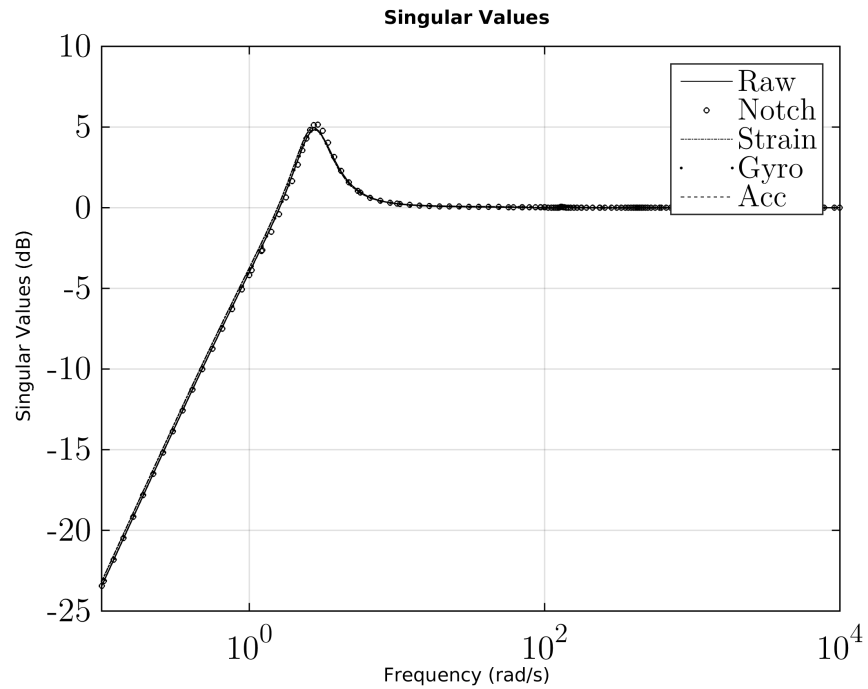


Figure 4.23: Sigma Plot of a_{zref} to $(a_{zref} - a_{zCG})$

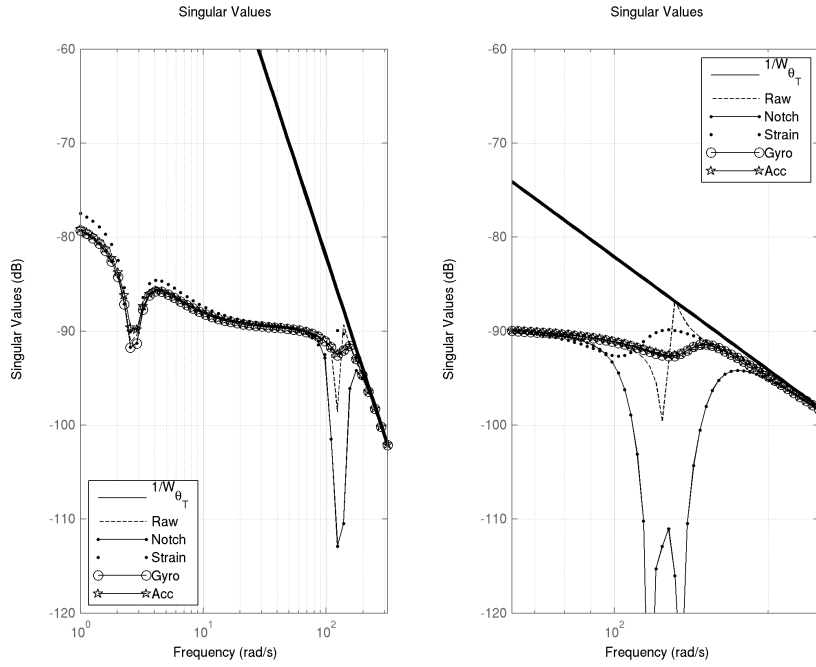


Figure 4.24: Singular Values of a_{zref} to θ_T

stays bounded under a reasonable threshold. The thrust vectoring demand is plotted on Figure 4.24 with respect to frequency.

None of these five architectures cross the threshold imposed by $1/W_{\theta_T}$. The “Notch” architecture has a thorough stop-band around the 1st bending mode natural frequency of 125 rad/s. The “Raw” architecture tangents this threshold without crossing it. The three active damping architectures keep a satisfactory margin. Similarly for the fins actuator, Figure 4.25 shows the fins deflection for the closed-loops performing active damping.

The “Strain” and the “Acc” architectures generate greater commands on the fins deflection at frequencies under 100 rad/s compared to the “Gyro” architecture. These closed-loop do not generate fins deflection at high frequencies.

4.5.3.2 Parasitic Effects

Bending vibrations are a source of parasitic actuations on the thrust vectoring. Indeed, the vibrations will generate parasitic signals in the sensors measurements then propagated through the controller and to the thrust vectoring. The bending vibrations are mostly generated by the rocket engine which thrust magnitude and orientation is very noisy. The parasitic actuations can be observed on the singular values from a perturbation on the thrust orientation to the actuated nozzles orientation on Figure 4.26. The “Raw” architecture with no vibration alleviation device is very sensitive to that

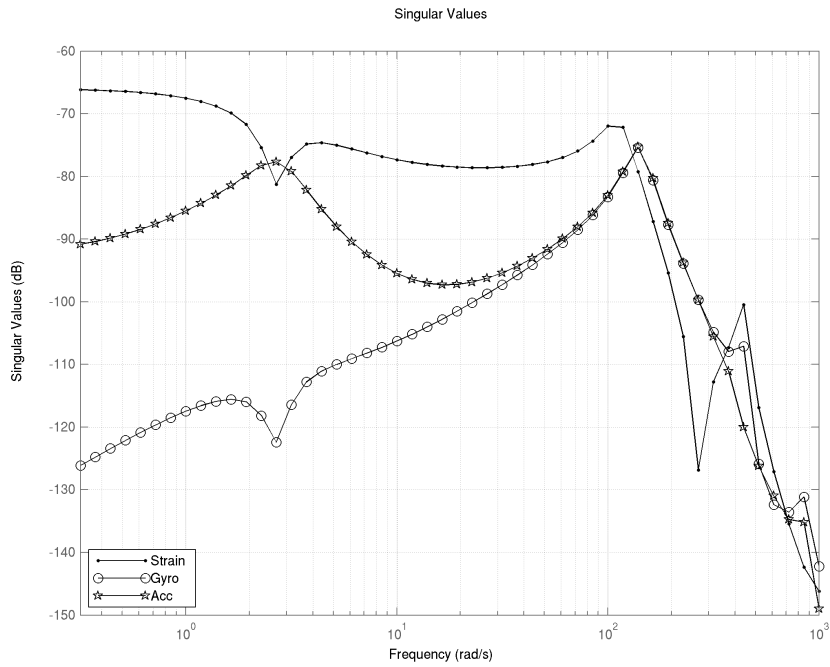


Figure 4.25: Singular Values of a_{zref} to δ_F

kind of perturbation. Indeed, the vibration noise can proliferate to the thrust vectoring actuation. The “Notch” architecture suppresses this noise with the notch filter without removing the vibrations. The active damping architectures “Strain”, “Gyro” and “Acc” suppress the vibrations directly. This parasitic actuation is significant for the “Raw” architecture. Indeed a perturbation on the thrust orientation of 1° at 125 rad/s brings a thrust vectoring parasitic actuation of 1.3°.

4.5.4 Bending Reduction

In the previous section, it has been seen that an architecture with a notch filter or with active damping have similar tracking performance, and a good rocket engine noise rejection. The difference between them appears when it comes to dynamic bending reduction.

4.5.4.1 Vibrations Alleviation

The active damping architectures have the advantage of reducing bending vibrations. ASTER-30 sensors pack is equipped with several tracking and attitude control sensors. They are greatly sensitive to vibrations and filtering always brings delays. The active damping will thoroughly reduce vibrations and hence improve tracking and attitude control.

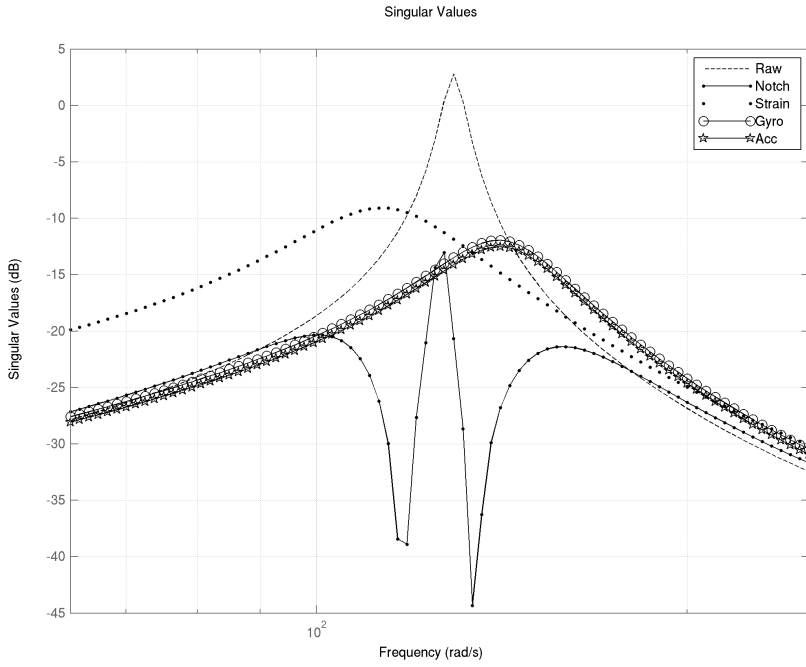


Figure 4.26: Singular Values of θ_{Tpert} to θ_T

The rocket engine creating a noisy thrust is the main source of bending vibrations. The singular values of this propagation is shown on Figure 4.27 where θ_{Tpert} is the noisy thrust deflection and a_{z83v} and q_{83v} are the vibration component of acceleration and pitch rate at sensors pack location. Indeed the two first architectures “Raw” and “Notch” do nothing to reduce these vibrations whereas the other three “Strain”, “Gyro” and “Acc” cut them down strongly.

4.5.4.2 Dynamic Stress Alleviation

By reducing bending oscillations, the active damping will also reduce stress due to dynamic deformations. The junction between the booster and the dart is located where the flexure due to the first bending mode is maximum. Therefore this link must be very stiff and resistant to flexure. With active damping, this link can be lighten and simplified. Figure 4.28 shows the strain reduction with active damping compared to non active damping next to the link. The source of vibrations is again the rocket engine thrust orientation noise.

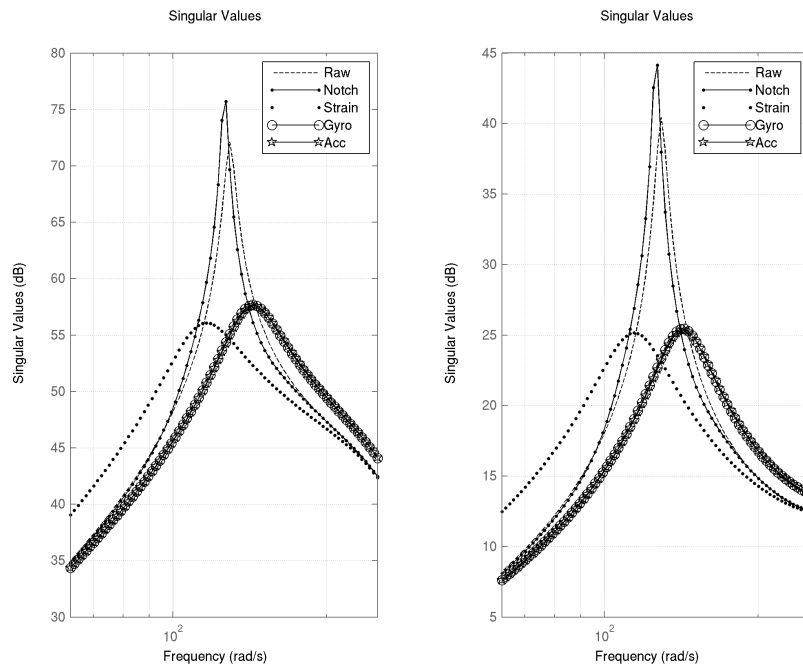


Figure 4.27: Singular Values of θ_{Tpert} to a_{z83v} (left) and q_{83v} (right)

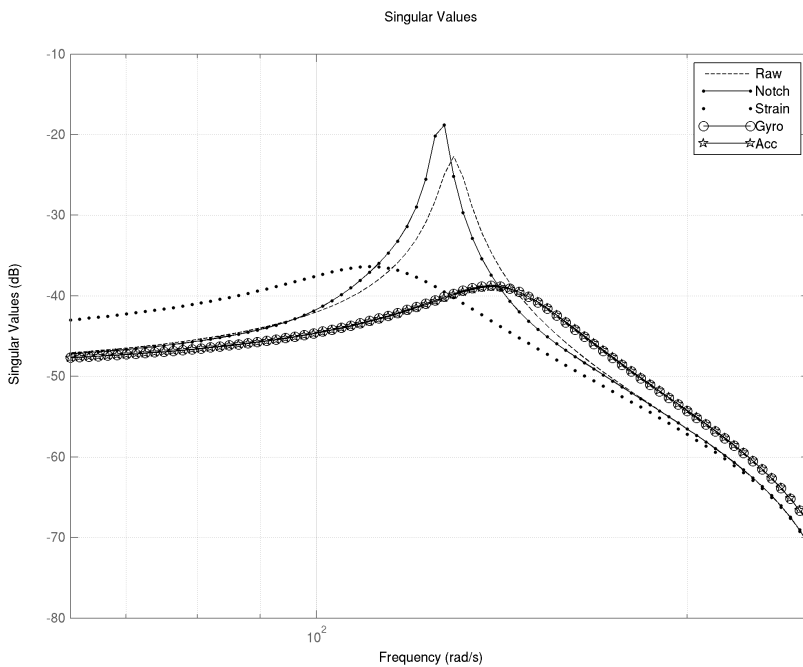


Figure 4.28: Singular Values of θ_{Tpert} to ε_{46}

Chapter 5

Results and Discussions

Chapter 6

Conclusions

References

- [1] Pierre Apkarian and Dominikus Noll. Nonsmooth H_∞ synthesis. *Automatic Control, IEEE Transactions on*, 51(1):71–86, 2006.
- [2] Moawwad El-Mikkawy and El-Desouky Rahmo. A new recursive algorithm for inverting general tridiagonal and anti-tridiagonal matrices. *Applied Mathematics and Computation*, 204(1):368–372, 2008.
- [3] Eugene L Fleeman. *Tactical missile design*. Amer Inst of Aeronautics &, 2006.
- [4] Wodek K Gawronski. *Dynamics and control of structures: A modal approach*. Springer Science & Business Media, 2004.
- [5] D Lesieutre, J Love, M Dillenius, and AB Blair Jr. Recent applications and improvements to the engineering-level aerodynamic prediction software misl3. In *Proceedings of the 40th AIAA Aerospace Sciences Meeting and Exhibit*, pages 2002–0275, 2002.
- [6] James Martin Prentis and Frederick A Leckie. *Mechanical vibrations: an introduction to matrix methods*. Longmans, 1963.